RSC Advances

PAPER

View Article Online
View Journal | View Issue

Cite this: *RSC Adv.*, 2025, **15**, 45480

Morphology-dependent synergy in high-performance MnO_2/activated carbon electrodes *via* facile dry-mixing

Xuefei Cao,[a] Xinran Liu,[b] Qinglong Zou[a] and Wei Sun *[b]

The pursuit of high-performance supercapacitors (SCs) often revolves around developing novel nanostructures through complex chemical synthesis, which poses challenges for scalable production. Herein, we demonstrate that exceptional electrochemical properties can be achieved by a simple dry-mixing of activated carbons (ACs) and manganese dioxide (MnO_2). A series of ACs with distinct morphologies were prepared and composited with petal-like MnO_2 clusters. We systematically investigated the profound impact of AC morphology on the synergistic effects with MnO_2. The optimal hybrid electrode, comprising spherical carbon (ACS-2.5) and 25 wt% MnO_2, delivered a superior gravimetric capacitance of 430.44 F g^{-1}, a remarkable volumetric capacitance of 357.27 F cm^{-3} and an outstanding capacitance retention of 93.41 ± 0.23% after 5000 cycles. Furthermore, this electrode achieved an exceptional energy density of 14.96 Wh kg^{-1} at a power density of 61 W kg^{-1}. Notably, the synergy was found to be highly morphology-dependent: a universal optimal MnO_2 ratio of ~25 wt% was identified for lamellar ACs, whereas the ideal ratio for spherical ACs increased with their diameter. Electrochemical impedance spectroscopy (EIS) and detailed mechanistic analysis revealed that MnO_2 acts as a multifunctional agent, serving as an interparticle conductive bridge and intraparticle spacer, thereby drastically reducing charge transfer resistance and enhancing ion diffusion. Critically, the incorporation of MnO_2 simultaneously increased the electrode compaction density, which is crucial for volumetric energy storage performance. This work provides fundamental insight into the structure–property relationship in hybrid electrodes and establishes a simple, scalable, and effective paradigm for designing high-performance energy storage devices by leveraging the synergy between conventional materials.

Received 3rd September 2025
Accepted 15th November 2025

DOI: 10.1039/d5ra06606a

rsc.li/rsc-advances

Introduction

The ever-growing demand for renewable energy and portable police electronic equipment has intensified the need for efficient energy storage systems that combine high power density, long cycle life, and rapid charging capabilities.[1–3] Supercapacitors (SCs), particularly electrical double-layer capacitors (EDLCs), have emerged as a critical technology to bridge the power/energy gap between conventional batteries and dielectric capacitors due to their ultra-fast charge–discharge rates and exceptional cycling stability.[4–7] Activated carbon (AC) remains the most prevalent commercial electrode material for EDLCs, prized for its high specific surface area (SSA), tunable porosity, good conductivity, and low cost.[8–10] However, the purely physical charge storage mechanism of ACs inherently limits their energy density. Furthermore, the highly porous nature of ACs, while beneficial for gravimetric performance, typically results in low electrode packing density, which severely compromises their volumetric capacitance—a critical metric for real-world applications where device size is a constraint.[11–13]

To overcome this limitation, intensive research has focused on integrating pseudocapacitive materials, such as transition metal oxides[14,15] and conducting polymers,[16–18] which offer faradaic reactions for higher specific capacitance and energy density. Among them, manganese dioxide (MnO_2) is a particularly promising candidate due to its high theoretical capacitance (~1370 F g^{-1}), natural abundance, low cost, and environmental friendliness.[19–21] However, despite its attractive theoretical value, the practical application of pure MnO_2 is severely hampered by its intrinsically low electrical conductivity, which leads to sluggish charge transfer kinetics, poor rate capability, and unsatisfactory utilization of active material.[22–24] This results in experimentally measured capacitances far below the theoretical expectation, alongside significant capacitance fading at high current densities.[25–27] Notably, MnO_2 possesses a significantly higher intrinsic density compared to highly

[a]*Criminal Investigation and Counter-Terrorism College, Criminal Investigation Police University of China, Shenyang 110854, China*

[b]*School of New Energy and Advanced Materials, Liaoning Petrochemical University, No. 1 West Dandong Street, Fushun, Liaoning, 113001, China. E-mail: sunwei@lnpu.edu.cn*

porous carbonaceous materials, presenting a compelling opportunity to enhance the often-overlooked volumetric performance of carbon-based electrodes.[28,29] Consequently, constructing MnO_2/carbon composite electrodes has become a mainstream strategy to synergistically combine the complementary advantages of both materials: the high-power density and excellent cycling stability from the conductive AC framework, which facilitates electron transport and provides a stable backbone, and the enhanced energy density from MnO_2.[30–32]

A prevalent trend in current research is the development of sophisticated hybrid nanostructures through *in situ* growth,[33,34] co-precipitation,[29,35] or electrodeposition.[36,37] While these methods can yield intimate contact between components, they often involve complex procedures, harsh conditions, and difficulties in precisely controlling the mass ratio of MnO_2, potentially hindering large-scale production and commercialization. In contrast, the simple physical mixing of pre-synthesized components is a highly scalable and industrially compatible technique. Nevertheless, it is often perceived as inferior for achieving strong synergistic effects, primarily due to the presumed poor interfacial contact and inefficient utilization of the pseudocapacitive material. This perception has led to its relative neglect in fundamental mechanistic studies. Crucially, the central question of how the intrinsic morphological characteristics of the AC substrate dictate the effectiveness of this simple mixing process and the resulting electrochemical synergy remains largely unexplored and poorly understood. We hypothesize that the perceived limitations of dry-mixing are not inherent to the method itself, but rather stem from a lack of understanding of the structure–property relationship between the carbon host and the metal oxide guest.

Herein, we address this critical knowledge gap by demonstrating that a facile dry-mixing method, when guided by a deep understanding of the carbon substrate's morphology, can yield MnO_2/AC hybrid electrodes with exceptional comprehensive performance, outstanding not only in gravimetric but also in volumetric metrics. We deliberately prepared two classes of ACs with contrasting morphologies: lamellar ACs derived from direct chemical activation of hydro-char and spherical activated carbons (ACSs) obtained through a pre-carbonization step. These were physically blended with hydrothermally synthesized MnO_2. Our work moves beyond simply reporting performance metrics; it provides a deep and systematic investigation into the morphology-dependent synergistic mechanisms in dry-mixed electrodes. The central findings reveal that the optimal MnO_2 mass ratio and the resulting enhancement mechanism are intrinsically linked to the host carbon's morphology and porous structure. A key highlight is the dual role of MnO_2: it acts as both high-density bridges and conductive spacers, effectively enhancing both gravimetric and volumetric capacitances. This fundamental understanding, corroborated by extensive electrochemical analysis including EIS fitting, illuminates the critical role of carbon substrate design. Our study challenges the notion that complex synthesis is a prerequisite for high performance. Instead, we offer a practical and insightful guide for selecting and optimizing commercially available carbons for simple manufacturing of next-generation hybrid SC electrodes with tailored properties, which is directly relevant to advanced applications like unmanned aerial vehicles (UAVs) for burst-power missions and specialized tactical equipment requiring reliable and rapid energy release.

Experimental section

Preparation of ACs

ACs were prepared *via* a technique route consisting of a hydrothermal synthesis (HTS) and a subsequent chemical activation. For HTS, 58 mL of glucose solution (20 wt%, 10 wt% and 2.5 wt% in concentration) was introduced into a 100 mL polytetrafluoroethylene-lined autoclave, followed by the addition of 2 mL of 1 mol per L H_2SO_4. The solution was thoroughly stirred and then sealed in a stainless-steel autoclave. The sealed system was placed in an oven and heated at 180 °C for 24 hours. Upon completion, the autoclave was cooled to room temperature, after which the resulting liquid and solid products were separated *via* vacuum filtration, with the solid product being collected. The filtered solid was subsequently dried in an oven at 90 °C for 24 hours, yielding brown hydro-char. According to the glucose concentration, the hydro-char was named as HC-20, HC-10 and HC-2.5, respectively. For the preparation of lamellar ACs, HC-20 was mixed with KOH in different KOH/hydro-char mass ratios (1 : 1, 3 : 1 and 5 : 1), which was then activated in the isothermal zone of a tube furnace (OTF-1200, Kejing, China) under the protection of continuous nitrogen gas flow. The activation process was programmed in three stages: (1) heating to 800 °C at a rate of 10 °C min^{-1}; (2) holding at 800 °C for 1 hour; and (3) cooling down naturally to room temperature. After cooling, the product was collected and neutralized with 1 mol per L hydrochloric acid, thoroughly washed with deionized water (DI water) for 5 times, and vacuum dried at 90 °C for 24 hours. The prepared ACs were labeled AC-1, AC-3, and AC-5 according to the corresponding KOH/hydro-char mass ratio for the activation. The precursor HC-20 was chosen for lamellar ACs due to its practical advantage of higher production yield. It is important to note that the lamellar morphology resulting from the direct KOH activation of hydro-char is determined by the KOH/hydro-char mass ratio,[5] not by the initial size of the hydro-char particles. The KOH activation temperature was set at 800 °C, as the temperature around 800 °C are widely recognized optimum for developing a high-specific-surface-area porous structure.[38,39] Our tests at higher temperatures (*e.g.*, 900–1100 °C) resulted in a degradation of specific surface area and pore volume, likely due to the collapse of the porous framework, a finding consistent with other reports on the thermal synthesis of porous materials.

In order to produce activated carbon spheres (ACSs). Prior to KOH activation, hydro-chars were subjected to a pre-carbonization treatment at 500 °C for 2 hours under a nitrogen flow in a tube furnace. A pre-carbonization temperature of 500 °C was selected as it was sufficient to stabilize the carbon spheres for subsequent activation;[40] higher pre-treatment temperatures offered no additional textural or electrochemical advantages while increasing energy consumption, which is an important factor for potential scale-up. Subsequently, KOH activation was conducted using a KOH/

hydro-char mass ratio of 1 : 1, followed by the same post-treatment procedures as previously described. Based on the glucose concentration used during the HTS, the ACSs were designated as ACS-20, ACS-10, and ACS-2.5, respectively.

Preparation of MnO_2

0.5 g of $KMnO_4$ and 0.1 g of $Fe_2(SO_4)_3$ were dissolved in 36 mL of DI water under magnetic stirring for 20 minutes until a homogeneous solution was obtained. The resulting solution was transferred into a 100 mL PTFE liner, followed by the addition of 1.6 mL of 1 mol per L H_2SO_4 and thorough mixing. After assembled in an autoclave, the HTS process was carried out in an oven at 120 °C for 24 hours. After cooling down to room temperature, and the solid product was collected by filtration and subsequently dried, yielding a black-brown MnO_2 solid.

Materials characterization

The morphology of the ACs and MnO_2 was analyzed using scanning electron microscopy (SEM, Hitachi S-4800, Japan). High-resolution transmission electron microscopy (HRTEM, JEM-2100F, Japan) was utilized to examine the microstructural features. Nitrogen adsorption–desorption isotherms were measured using an Autosorb-IQ2-MP system (Quantachrome, USA) to assess the specific surface area, pore volume, and pore size distribution. The specific surface area was calculated based on the Brunauer–Emmett–Teller (BET) method, the total pore volume was determined at a relative pressure of 0.99, and the pore size distribution was derived from the slit-pore non-local density functional theory (NLDFT) equilibrium model. Raman spectroscopic analysis was conducted on a DXR spectrometer (Thermo Scientific, USA) with a 532 nm excitation laser. The crystal structures of the ACs and MnO_2 were further investigated by X-ray diffraction (XRD) using an X-ray powder diffractometer (D8 Advance, Bruker, Germany). X-ray photoelectron spectroscopy (XPS) analysis was conducted on an ESCALAB Xi^+ (Thermo Scientific, USA).

Fabrication of composite electrode and assemble of symmetric SC

The electrodes were fabricated using a dry-mixing method. MnO_2 and AC were blended in varying proportions as main electrode material, followed by the addition of PTFE powder (serving as binder) and carbon black powder (serving as conductive agent). The mass ratio of main electrode material, binder and conductive agent is fixed at 80 : 15 : 5. The mixture was heated at 110 °C for 1 h and then grounded into a thin sheet, which was then further thinned and flattened using a rolling machine, resulting in a uniform thickness of 0.15 mm. Circular electrode discs with a diameter of 10 mm were then punched from the sheet. The mass of each electrode disc was accurately measured using a microbalance (accuracy: 0.01 mg). The mass loading of the active material on a single electrode typically ranged from 3.0 to 4.0 mg cm^{-2}, corresponding to a total active material mass of 2.4 to 3.1 mg per electrode disc (diameter = 10 mm). The compaction density of the electrode, ρ was calculated based on the mass, m and volume, V of the cylindrical electrode disc by $\rho = m/V$, where the volume V was calculated from the geometric dimensions (radius = 5 mm, thickness = 0.15 mm) measured by a micrometer screw gauge. The reported compaction density for each composition is the average value obtained from at least three independently fabricated electrode discs. Symmetric SCs were assembled in CR2032-type coin cells with two identical electrodes. The geometric area of each electrode was 0.785 cm^2 (diameter = 10 mm). A piece of glass fiber filter (Whatman GF/A) with a thickness of ~0.26 mm was used as the separator. Approximately 150 μL of 1 mol per L KOH aqueous solution was used as the electrolyte for each cell. The assembly was performed in ambient atmosphere. All electrochemical measurements were conducted at room temperature.

Electrochemical measurements

The electrochemical performances were tested on a Vertex-one electrochemical workstation (Ivium, Netherland). The cyclic voltammetry (CV) and galvanostatic charge–discharge (GCD) measurements within a voltage window of 0–1 V, at various scan rates and current densities. Electrochemical impedance spectroscopy (EIS) was conducted with a sinusoidal perturbation amplitude of 10 mV over a frequency range of 10^6 to 10^{-2} Hz under open-circuit voltage.

The gravimetric capacitance, C_g and volumetric capacitance, C_v were calculated from the discharge portion of the GCD curves using the eqn (1) and (2), respectively:

$$C_g = \frac{2I}{m}\left(\frac{dV}{dt}\right)^{-1} \quad (1)$$

$$C_v = C_g \times \rho \quad (2)$$

where I is the discharge current, m is the mass loading of active materials, dV/dt is the slope of the discharge curve after the IR drop, and ρ is the compaction density of each electrode which is calculated based on the mass and volume of the electrode.

The energy density, E (Wh kg^{-1}) and power density, P (W kg^{-1}) were calculated based on the equations below:

$$E = \frac{1}{8} \times \frac{1}{3.6} \times C_g V^2 \quad (3)$$

$$P = \frac{E}{\Delta t} \quad (4)$$

where V is the GCD operating voltage window (1 V), and Δt is the discharge time.

All electrochemical data (C_g, C_v, *etc.*) reported in this work are the average values obtained from at least three independently fabricated electrodes for each composition. The error bars in the figures and the standard deviations in the tables represent the reproducibility of the electrode preparation and measurement.

Results and discussion

Materials characterization

Fig. 1 illustrates the morphological characteristics of the as-prepared ACs and the distribution of MnO_2 in the optimal

hybrid electrodes. It is well-established that hydro-char derived from small-molecule saccharides *via* HTS typically exhibits a well-defined spherical morphology.[41] As observed in Fig. 1a–c, direct KOH activation of hydro-char leads to the formation of lamellar ACs with an interconnected network. With increasing KOH/hydro-char mass ratios, the number of voids within the network progressively decreases, while their size significantly increases. The average void width in AC-1 is predominantly below 2 μm, whereas voids in AC-3 are slightly larger than 2 μm, and those in AC-5 generally exceed 2.5 μm. These results demonstrate that the morphology of the AC can be effectively controlled by adjusting the amount of activating agent. As shown in Fig. 1d–f, the sphere diameter exhibits a significant increase with higher glucose concentration during the HTS reaction (8.82 ± 1.25 μm for ACS-20, 6.28 ± 0.85 μm for ACS-10, and 2.96 ± 0.25 μm for ACS-2.5). Fig. 1g reveals that the synthesized MnO_2 displays a spherical morphology composed of petal-like clusters, with an average cluster diameter of approximately 1.25 ± 0.32 μm. A magnified view of an individual cluster demonstrates that the petal-like nanosheets possess a uniform thickness on the order of several nanometers.

The morphological evolution and distribution of MnO_2 within the composite electrodes by the dry-mixing are presented in Fig. 1h and i. Notably, the mechanical processing involved in electrode fabrication intentionally breaks down both the lamellar AC-5 and the petal-like MnO_2 clusters into smaller fragments (Fig. 1h). This structural reorganization, rather than being detrimental, creates a more densely packed architecture. Crucially, the EDX elemental mapping reveals that the resulting MnO_2 fragments effectively fill the voids within the carbon matrix (highlighted by yellow circles, as an intraparticle bridges) and simultaneously coat the carbon fragments (highlighted by blue circles, as interparticle spacers). For the spherical ACS-2.5 composite (Fig. 1i), the ACSs maintain their integrity remarkably well, while the MnO_2 fragments are dispersed and coat the

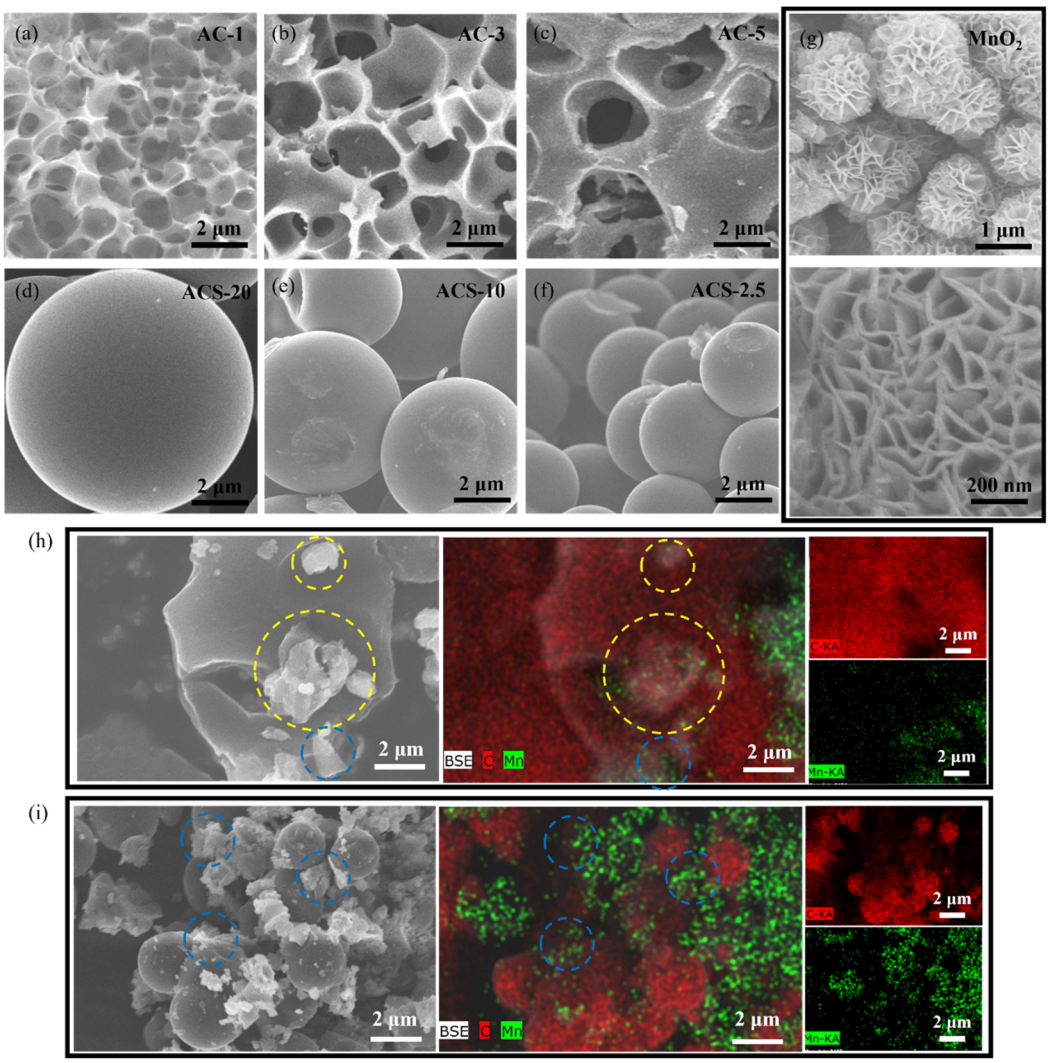

Fig. 1 SEM images and corresponding EDX elemental maps of the prepared ACs and representative composite electrodes: (a) AC-1, (b) AC-3, (c) AC-5, (d) ACS-20, (e) ACS-10, (f) ACS-2.5, (g) MnO_2, (h) AC-5/25% MnO_2 composite with C and Mn maps, and (i) ACS-2.5/25% MnO_2 composite with C and Mn maps.

surface of the spheres, primarily forming interparticle bridges (blue circles) between them. Additional SEM images of the composite are shown in Fig. S1 in SI.

The microstructure of ACs with distinct morphologies and MnO_2 was characterized by high-resolution transmission electron microscopy (HRTEM). As revealed in Fig. 2a–c, the lamellar AC exhibits relatively thin edges. In contrast, due to their spherical morphology, the ACS samples shown in Fig. 2d–f possess significantly thicker edges. All ACs lack discernible crystalline lattice structures, indicating that the KOH-activated ACs are predominantly amorphous. Furthermore, HRTEM analysis reveals the presence of irregular slit-shaped pores ranging from nano- to sub-nanometer scales within the ACs. Comparative examination of Fig. 2a–c indicates that ACs prepared with higher KOH/hydro-char mass ratios possess relatively larger pore sizes. The TEM image in Fig. 2g demonstrates that the MnO_2 exhibits a spherical cluster structure composed of nanosheets, consistent with the SEM observations. HRTEM of an individual MnO_2 cluster (Fig. 2h) reveals a well-defined crystalline lattice structure. Measurement and calculation confirm that the observed lattice fringes correspond to the (0 0 1) crystallographic plane of MnO_2.

The pore structures of the ACs were further characterized using N_2 adsorption–desorption analysis. As evidenced by the N_2 adsorption–desorption isotherms of the lamellar ACs (Fig. 3a), AC-1, prepared with a KOH/hydro-char mass ratio of 1 : 1, exhibits a characteristic Type I isotherm. This suggests monolayer adsorption dominates and confirms AC-1 is primarily microporous. With increasing KOH/hydro-char mass ratios, the inflection point (knee) following the initial rapid adsorption becomes notably broader for AC-3, indicating a wider pore size distribution. Conversely, AC-5 displays a composite isotherm featuring characteristics of both Type I and Type IV, signifying a higher proportion of mesopores. The pore size distribution (PSD) curves in Fig. 3b reveal that micropores predominate in AC-1 and AC-3, while AC-5 exhibits a notable increase in mesopore volume. For the spherical ACSs activated under an identical KOH/hydro-char mass ratio (1 : 1), the adsorption–desorption isotherms (Fig. 3c) all display typical Type I behavior, although ACS-2.5 shows a slightly broader knee. The PSDs of the ACSs (Fig. 3d) demonstrate that, compared to the lamellar ACs, the ACSs possess smaller pores predominantly concentrated within the 0.5–1 nm range. This observation indicates that the pre-carbonization step prior to activation enhances the stability of the carbon framework, thereby hindering the formation of larger pores.

Table 1 summarizes the surface properties of the ACs prepared under different conditions. As the KOH/hydro-char mass ratio increases, the specific surface area (SSA), total pore volume, and mesopore ratio of the ACs show significant enhancement. The maximum SSA achieved was 2910 $m^2\ g^{-1}$, accompanied by a mesopore ratio of 37.8%. In contrast, under identical KOH activation conditions (mass ratio 1 : 1), the ACSs prepared with the additional pre-carbonization step exhibit lower SSAs compared to AC-1. Furthermore, a slight increase in SSA, pore volume, and mesopore ratio is observed as the sphere diameter decreases.

The crystalline structures and graphitic nature of the as-prepared materials were thoroughly characterized by X-ray diffraction (XRD) and Raman spectroscopy, with the results

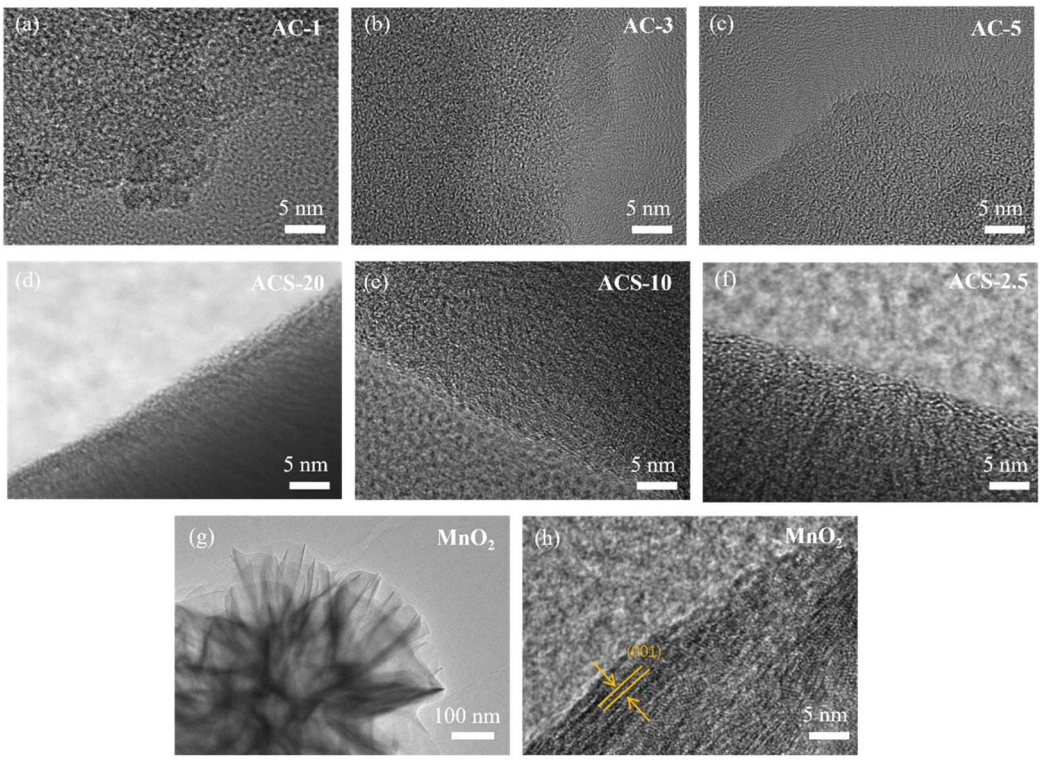

Fig. 2 HRTEM images of the prepared ACs and MnO_2: (a) AC-1, (b) AC-3, (c) AC-5, (d) ACS-20, (e) ACS-10, (f) ACS-2.5, and (g and h) MnO_2.

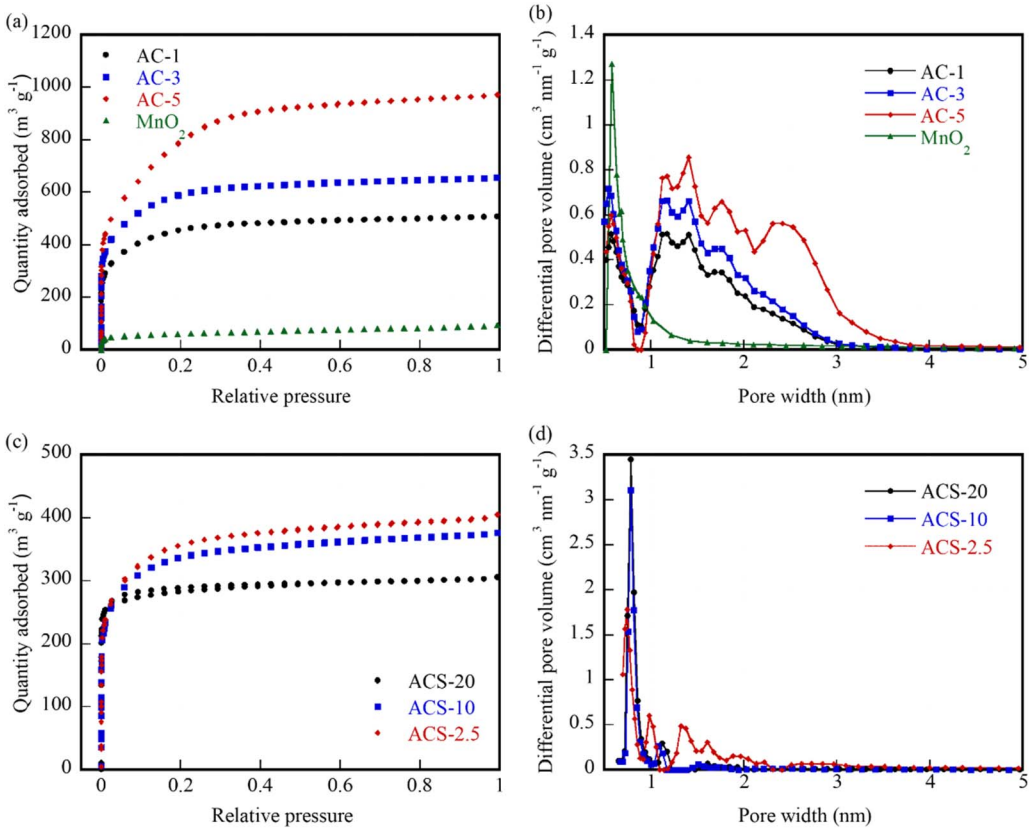

Fig. 3 N_2 adsorption–desorption isotherms for: (a) lamellar ACs and (c) ACSs; pore width distribution for (b) lamellar ACs and (d) ACSs.

summarized in Fig. 4. The XRD patterns of all ACs, both lamellar AC-*x*s and spherical ACSs, exhibit nearly identical profiles (Fig. 4a and b). Two broad and low-intensity diffraction peaks are observed at approximately 21° and 43° (2θ), corresponding to the (0 0 2) and (1 0 0) planes of graphitic carbon, respectively. The considerable broadening of these peaks and the absence of any other sharp features confirm the highly amorphous nature of all ACs, irrespective of their morphology (lamellar or spherical) or specific porous architecture. This indicates that the KOH activation process, while successfully developing an extensive porous network, did not induce significant graphitization, preserving the disordered carbon structure essential for high specific surface area. In stark contrast, the XRD pattern of the synthesized MnO_2 (Fig. 4c) displays a set of distinct diffraction peaks. A strong and sharp peak is observed at approximately 12.1°, accompanied by several weaker but discernible peaks near 24.5°, 37.5°, and 67.5°. This pattern is unequivocally indexed to the birnessite-type manganese dioxide (δ-MnO_2) (JCPDS card no. 80-1098).[42] The dominant (0 0 1) peak indicates a preferred orientation with the layered structure stacked parallel to the substrate. However, the noticeable broadening of the peaks at 37.5° and 67.5° suggests that the crystalline domains are nanoscale in size and may possess a certain degree of structural disorder within the layers. For the ACS-2.5/25% MnO_2 and AC-5/25% MnO_2 composites, the XRD patterns (Fig. 4c) present distinct features from their individual components. The characteristic peaks of δ-MnO_2 are substantially attenuated, with the peak at ~67.5°

Table 1 Surface texture of the ACs

Sample	S_{BET} (m^2 g^{-1})	Total pore volume (mm^3 g^{-1})	Pore volume fraction (%)		I_D/I_G
			Micropore	Mesopore	
AC-1	1423 ± 23	0.72 ± 0.01	83.2 ± 0.3	16.8 ± 0.3	0.96
AC-3	2163 ± 44	1.02 ± 0.02	78.8 ± 0.7	21.2 ± 0.7	1.00
AC-5	2910 ± 62	1.52 ± 0.03	62.2 ± 0.8	37.8 ± 0.8	1.08
ACS-20	944 ± 18	0.49 ± 0.01	91.8 ± 0.1	8.2 ± 0.1	0.98
ACS-10	1186 ± 21	0.58 ± 0.01	89.5 ± 0.2	10.5 ± 0.2	0.99
ACS-2.5	1211 ± 25	0.61 ± 0.02	88.4 ± 0.2	11.6 ± 0.2	1.01
MnO_2	218 ± 11	0.114 ± 0.01	93.3 ± 0.2	6.7 ± 0.2	—

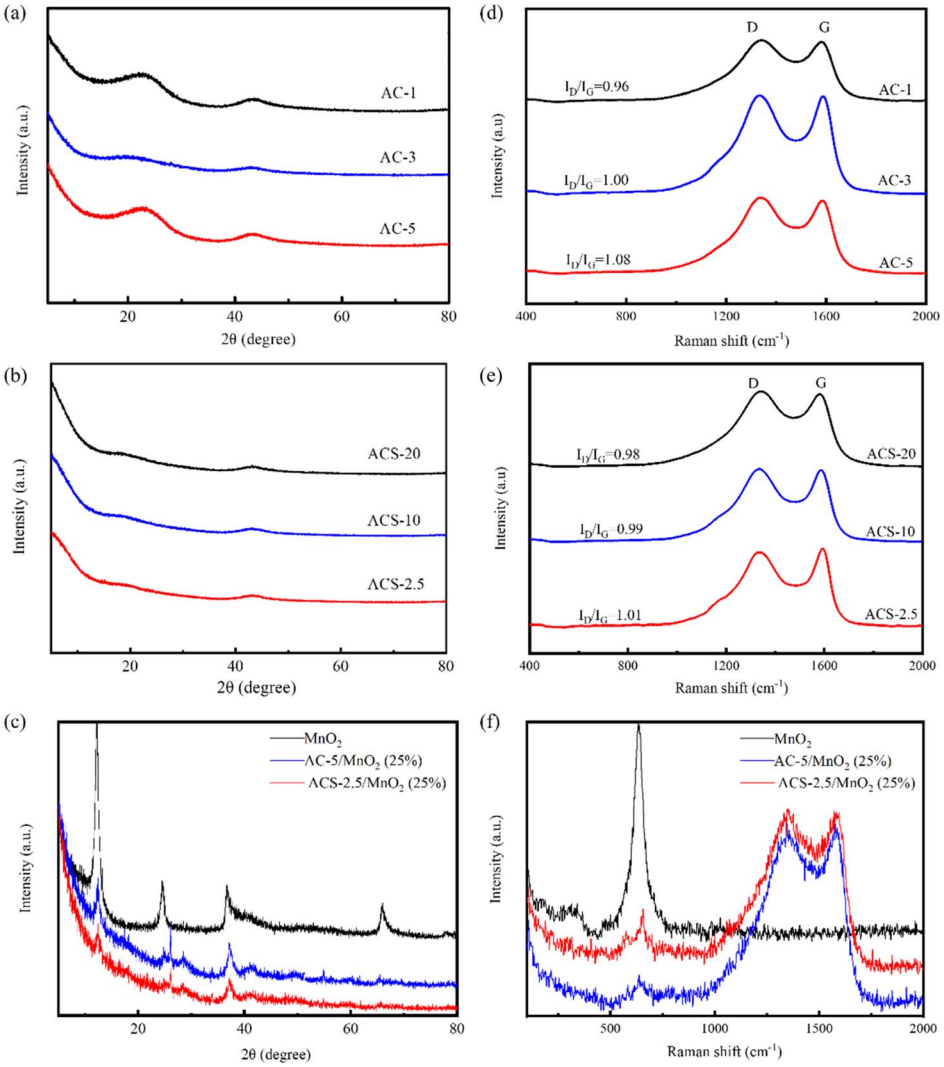

Fig. 4 XRD patterns of: (a) AC-*x*s, (b) ACSs, and (c) MnO_2 and optimal composite electrodes; Raman spectra of: (d) AC-*x*s, (e) ACSs, and (f) MnO_2 and optimal composite electrodes.

vanishing entirely and the intensities of the other peaks (*e.g.*, at ~12.1°, 24.5°, and 37.5°) becoming significantly less prominent. Concurrently, the broad diffraction humps of the amorphous ACs also become less discernible against the background. This overall attenuation of the crystalline signatures is attributed to the unique microstructure of the dry-mixed composites. The dry-mixing process itself likely fragments the MnO_2 clusters into smaller crystallites, a reduction in crystalline size leads to peak broadening and a concomitant decrease in intensity. This effect, combined with the dilution effect from the high dispersion of these nanocrystalline MnO_2 within the dominant amorphous carbon matrix, profoundly diminishes the diffraction intensity. Furthermore, the MnO_2 fragments intimately integrate with the carbon framework. This integration effectively disrupts the long-range order and further shields the diffraction from both components. These observations provide direct structural evidence for the formation of a highly homogeneous and tightly interwoven composite architecture through simple dry-mixing.

The Raman spectra of the ACs provide further insight into their graphitic structure (Fig. 4d and e). All AC samples show two characteristic bands: the D band at ~1350 cm^{-1}, representing the breathing mode of A_1g symmetry arising from disordered or defective sp^3 carbon, and the G band at ~1580 cm^{-1}, associated with the in-plane vibrational mode of E_{2g} symmetry in ideal sp^2-hybridized graphitic domains.[43,44] The intensity ratio of these bands (I_D/I_G) is a semi-quantitative indicator of the defect density within the carbon structure. As listed in Table 1, the I_D/I_G ratios for all samples are close to 1.00, confirming a consistently high level of structural disorder across all ACs, which is consistent with the XRD results. A slight but measurable increase in the I_D/I_G ratio is observed for the AC-*x* series with higher KOH/hydro-char mass ratios (from AC-1 to AC-5), indicating that more intensive activation introduces a greater number of defects and nanopores into the carbon framework. Conversely, the ACSs, activated under identical conditions (1 : 1 ratio), exhibit very similar I_D/I_G values regardless of their sphere size, implying a comparable level of

graphitization and defect density. The Raman spectrum of the synthesized MnO_2 (Fig. 4f) corroborates the XRD findings. The spectrum is dominated by a strong, yet broadened, peak centered at 632 cm^{-1}, which is the fingerprint Raman mode for birnessite-type MnO_2, assigned to the symmetric stretching vibration (ν_3) of the Mn–O bonds. The significant broadening of this primary peak is a direct manifestation of the nanocrystalline nature and structural defects within the material. This defective crystalline structure, while potentially detrimental to its intrinsic electrical conductivity, is pivotal for its role as a morphological modifier in the composite electrodes, facilitating integration with the carbon matrix. The Raman spectra of the composites (Fig. 4f) exhibit the superimposed features of both components: the D and G bands from the ACs and the characteristic peak at ~632 cm^{-1} from the δ-MnO_2. These findings collectively confirm the successful integration of both materials in the composite electrodes and support a physical synergistic effect rather than a chemical reaction.

Fig. 5a reveals a clear increase in the compaction density of the electrodes incorporating lamellar ACs as the mass fraction of MnO_2 increases. For electrodes fabricated using pure ACs (MnO_2 wt% = 0), the compaction density exhibits a significant reduction with increasing KOH/hydro-char mass ratio. This trend is primarily attributed to the combined effect of two factors: variations in total pore volume and distinct packing behaviors resulting from the differing AC morphologies. Notably, the disparity in density among electrodes composited with different ACs gradually diminishes as the proportion of MnO_2 increases. Regarding the spherical activated carbons (ACSs) activated under an identical KOH/hydro-char mass ratio (1 : 1), ACS-2.5, despite possessing the highest pore volume, demonstrates the highest compaction density (Fig. 5b). This phenomenon is chiefly due to the smaller sphere diameter enabling tighter packing. Furthermore, the compaction density of the electrodes composited with ACSs also progressively increases with higher MnO_2 mass fractions. These results collectively demonstrate the significant role of MnO_2 in enhancing the electrode compaction density, thereby contributing favorably to the improvement of the volumetric capacitance.

Electrochemical performances

Fig. 6 compares the electrochemical performance of SCs employing AC-5/MnO_2 composite electrodes with varying mass ratios. As shown in Fig. 6a, the cyclic voltammetry (CV) curve of the pure MnO_2 electrode (100 wt% MnO_2) at 100 mV s^{-1} exhibits a slender shape. This indicates suboptimal capacitive behavior at relatively high scan rates. The small enclosed area further confirms its low specific capacitance. In contrast, pure AC-5 displays a nearly ideal quasi-rectangular CV profile, signifying significantly superior capacitive characteristics and electrical conductivity. For electrodes containing 50 wt% and 75 wt% MnO_2, the CV curves show intermediate rectangularity and enclosed areas between those of pure AC-5 and pure MnO_2. Notably, the electrode with 25 wt% MnO_2 exhibits the most ideal CV shape and the largest enclosed area, demonstrating enhanced current–voltage (I–V) response kinetics and higher specific capacity compared to pure AC-5.

The absence of pseudocapacitive features in the cyclic voltammetry curves, even for the pure MnO_2 electrode, is a critical observation that underscores the inherent electrochemical limitations of the synthesized birnessite-type MnO_2 under these experimental conditions. This behavior can be attributed to a combination of its intrinsic material properties and the resulting electrode architecture: the nanocrystalline, highly defective structure, evidenced by broadened XRD peaks and broad Raman band, severely compromises both electronic conductivity and ionic diffusion kinetics, fundamentally limiting the rate of the faradaic intercalation process that is characteristic of crystalline birnessite. Furthermore, in the pure MnO_2 electrode, the absence of a conductive carbon matrix exacerbates the issue, leading to high internal resistance and inefficient charge collection, while the use of a strong alkaline electrolyte (1 M KOH) may induce surface passivation or partial dissolution, further suppressing electrochemical activity. Consequently, the electrochemical response is overwhelmingly dominated by the physical and interfacial characteristics of the materials, with the MnO_2 primarily contributing through its role as a structural modifier. In the composite electrodes, this manifests as a remarkably ideal EDLC behavior, where the

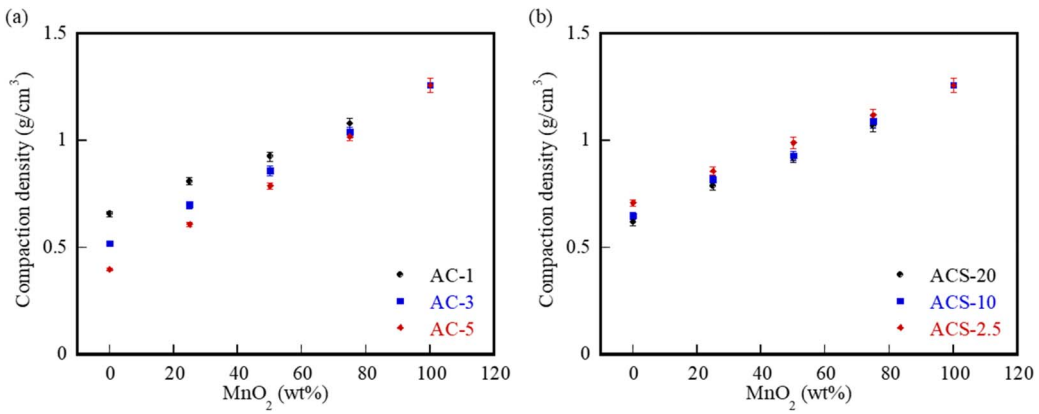

Fig. 5 Variation of compaction density with weight percentage of MnO_2 for: (a) lamellar ACs activated with different KOH/hydro-char mass ratios and (b) ACSs with different sphere sizes.

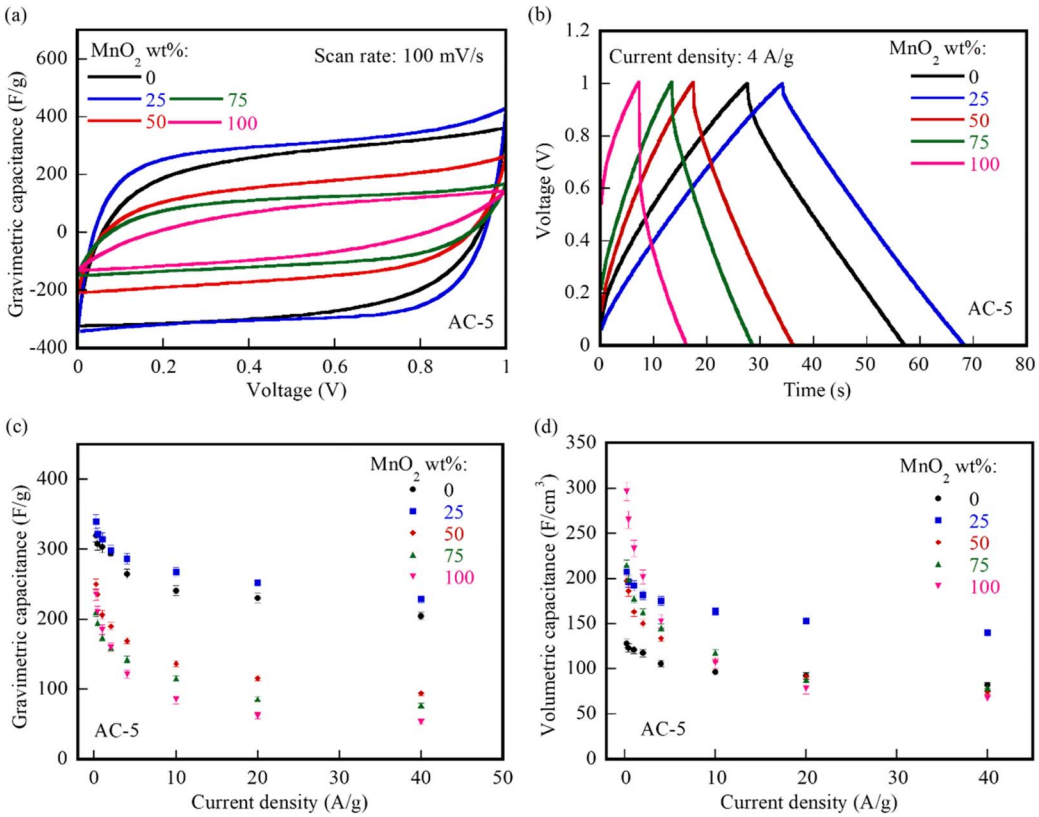

Fig. 6 Electrochemical performances of SCs based on the composite of AC-5 and MnO_2 in different mass ratios: (a) CV curves at 100 mV s^{-1}, (b) GCD curves at 4 A g^{-1}, (c) variation of gravimetric capacitance with current density, and (d) variation of volumetric capacitance with current density.

instantaneous charging of the highly conductive AC framework is further enhanced by the MnO_2's ability to improve electrode density and ion transport pathways.

Galvanostatic charge–discharge (GCD) curves at 4 A g^{-1} (Fig. 6b) reveal that increasing the MnO_2 mass fraction generally degrades the linearity, symmetry, and IR drop, suggesting compromised electrochemical reversibility and increased internal resistance. However, the 25 wt% MnO_2 composite electrode displays the optimal GCD curve shape with the smallest IR drop, indicating superior electrochemical performance at this composition, consistent with the CV results.

Fig. 6c compares the specific gravimetric capacitance across different MnO_2 loadings. The pure MnO_2 electrode exhibits lower specific capacitance than pure AC-5, along with significantly inferior rate capability (capacitance retention at 40 A g^{-1}). Reducing the MnO_2 proportion enhances the composite's gravimetric capacitance, with the 25 wt% MnO_2 electrode achieving the highest gravimetric capacitance (340 F g^{-1} at 0.2 A g^{-1}) and rate performance (0.67 in capacitance retention at 40 A g^{-1}), even exceeding pure AC-5. As depicted in Fig. 6d, the pure MnO_2 electrode achieves the highest initial volumetric capacitance at low current densities due to its high compaction density. However, its poor rate capability results in drastically reduced volumetric capacitance at high current densities. Conversely, the 25 wt% MnO_2 composite electrode maintains superior volumetric capacitance across all tested current densities, benefiting from its high gravimetric capacitance and excellent rate capability.

Fig. S2 and S3 in SI present the electrochemical performance of composite electrodes based on AC-1 and AC-3 with varying MnO_2 mass fractions. Consistent with the AC-5 results, both AC types exhibit optimal electrochemical performance at 25 wt% MnO_2. To further validate the optimal mass ratio, we synthesized and tested composites with intermediate loadings of 12.5 wt% and 37.5 wt% MnO_2 for the lamellar AC-*x*s series. As shown in Fig. S4–S6, both the 12.5 wt% and 37.5 wt% composites delivered lower gravimetric and volumetric capacitances compared to the 25 wt% benchmark almost across all tested current densities. This result confirms that 25 wt% is indeed the optimal loading for maximizing the synergy in lamellar ACs.

Table 2 summarizes the capacitance and rate capability metrics for composite electrodes based on the three lamellar ACs. The gravimetric capacitance and rate capability of pure AC-*x*s electrodes exhibit significant enhancement with increasing KOH/hydro-char mass ratios, primarily governed by their more developed pore architectures. Higher specific surface areas (Table 1) provide increased accessible adsorption sites, while elevated mesopore ratios establish efficient ion transport highways. Furthermore, the optimized hierarchical porosity enables superior pore utilization efficiency, collectively contributing to the improved gravimetric capacitance and

Table 2 Specific capacitance and rate capability of AC-*x* based composite electrode[a]

Sample	AC-1			AC-3			AC-5		
	$C_{0.2}$			$C_{0.2}$			$C_{0.2}$		
MnO_2 wt%	C_g (F g^{-1})	C_v (F cm^{-3})	$C_{40}/C_{0.2}$	C_g (F g^{-1})	C_v (F cm^{-3})	$C_{40}/C_{0.2}$	C_g (F g^{-1})	C_v (F cm^{-3})	$C_{40}/C_{0.2}$
0	235.30 ± 7.06	154.83 ± 3.74	0.35 ± 0.02	250.00 ± 7.50	140.00 ± 4.50	0.54 ± 0.02	320.00 ± 9.60	128.00 ± 6.62	0.64 ± 0.03
25	247.30 ± 7.42	200.81 ± 4.97	0.39 ± 0.03	266.67 ± 8.34	175.00 ± 6.17	0.55 ± 0.03	340.00 ± 10.20	183.60 ± 8.47	0.67 ± 0.03
50	200.00 ± 6.08	185.00 ± 4.80	0.33 ± 0.02	235.30 ± 7.06	218.66 ± 6.14	0.34 ± 0.03	250.00 ± 7.50	165.00 ± 7.20	0.38 ± 0.02
75	166.67 ± 5.28	90.00 ± 4.85	0.33 ± 0.02	160.00 ± 4.80	155.20 ± 4.75	0.25 ± 0.02	210.53 ± 6.32	170.52 ± 7.07	0.37 ± 0.01
100	235.30 ± 8.12	296.48 ± 10.23	0.23 ± 0.01	235.30 ± 8.12	296.48 ± 10.23	0.23 ± 0.01	235.30 ± 8.12	296.48 ± 10.23	0.23 ± 0.01

[a] The "100 wt% MnO_2" refers to a pure MnO_2 electrode (*i.e.*, the "main electrode material" is 100% MnO_2, mixed with PTFE and carbon black in the fixed 80 : 15 : 5 ratio) and is the same across all AC samples, representing the average performance of this specific electrode.

charge–discharge kinetics. However, this highly porous structure compromises electrode density, resulting in suboptimal volumetric capacitance for AC-5.

Fig. 7 compares the electrochemical performance of composite electrodes incorporating various AC-*x*s materials at their optimal MnO_2 mass loading (25 wt%). As depicted in Fig. 7a, the hybrid electrodes based on AC-3 and AC-5 exhibit favorable rectangular-like CV profiles under this composition, indicative of efficient capacitive charge storage. In contrast, the AC-1 composite demonstrates a comparatively distorted CV response. GCD curves recorded at 4 A g^{-1} (Fig. 7b) reveal well-defined symmetric triangular shapes with minimal IR drops for all three hybrid electrodes, signifying low internal resistance and highly reversible charge–discharge behavior. Analysis of the gravimetric capacitance (Fig. 7c) demonstrates that the AC-5/MnO_2 hybrid achieves substantially higher capacitance than its counterparts. This enhancement is primarily contingent upon the intrinsically superior charge-storage capability of the AC-5 matrix. However, owing to the inverse relationship between electrode density and gravimetric capacitance across the AC series, the disparity in volumetric capacitance (Fig. 7d) is markedly reduced. Despite this convergence, the AC-5-based

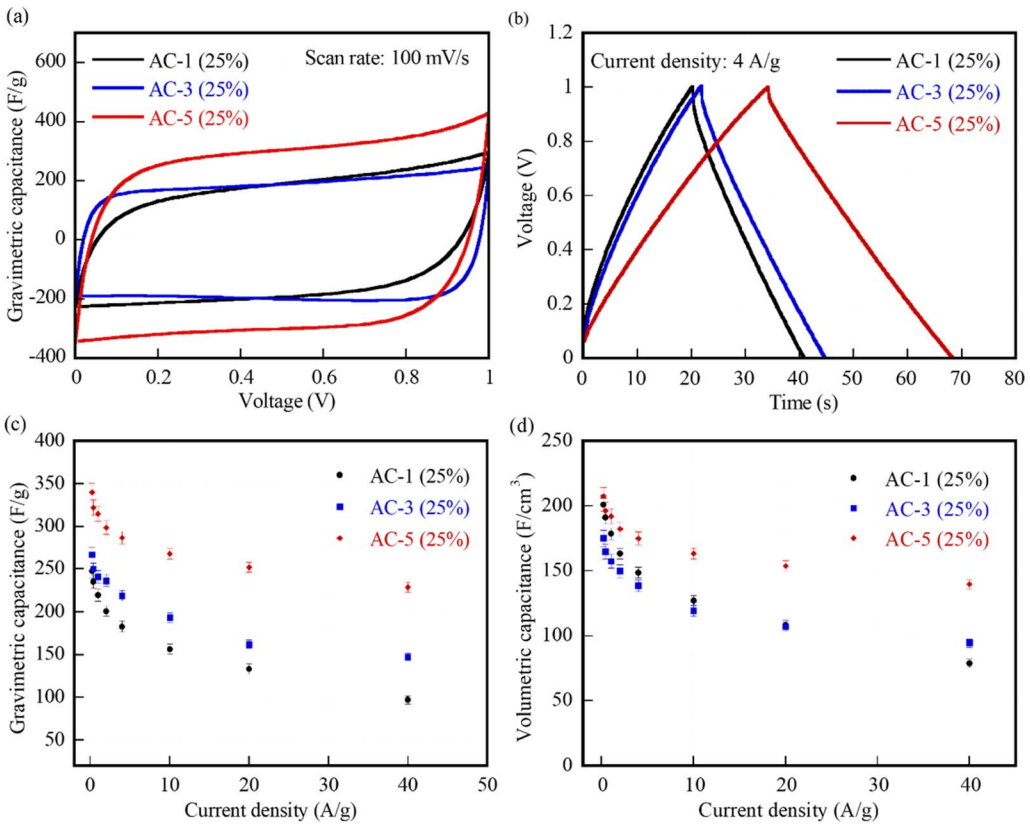

Fig. 7 Comparison of the electrochemical performances of AC-*x*s-based composite electrode at a MnO_2 mass ratio of 25%: (a) CV curves at 100 mV s^{-1}, (b) GCD curves at 4 A g^{-1}, (c) variation of gravimetric capacitance with current density, and (d) variation of volumetric capacitance with current density.

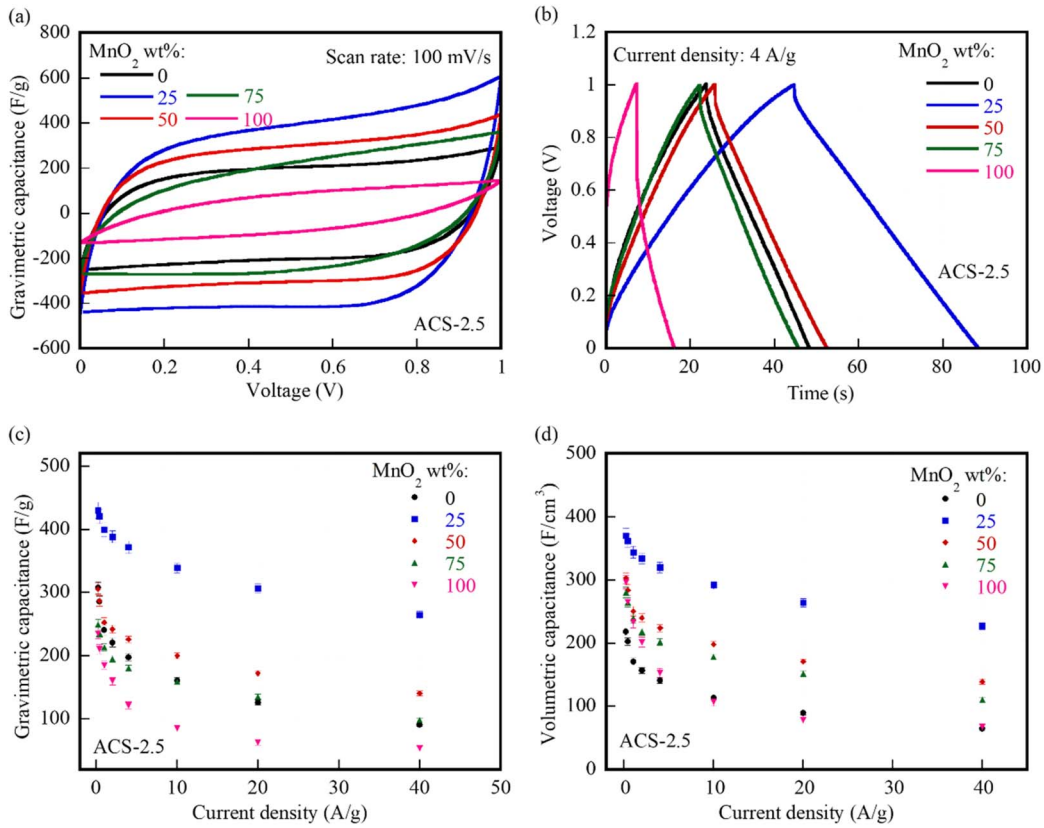

Fig. 8 Electrochemical performances of SCs based on the composite of ACS-2.5 and MnO_2 in different mass ratios: (a) CV curves at 100 mV s^{-1}, (b) GCD curves at 4 A g^{-1}, (c) variation of gravimetric capacitance with current density, and (d) variation of volumetric capacitance with current density.

composite maintains the highest volumetric capacitance among the evaluated systems.

Fig. 8 details the electrochemical performance of composite electrodes incorporating carbon spheres (ACS-2.5) with varying MnO_2 mass fractions. CV profiles (Fig. 8a) indicate that all composites except those with 75 wt% and 100 wt% (pure MnO_2) retain near-ideal rectangular shapes, signifying efficient capacitive behavior. Notably, electrodes containing 25 wt% and 50 wt% MnO_2 exhibit substantially larger enclosed CV areas than pristine ACS-2.5, demonstrating enhanced charge-storage capacitance. GCD curves at 4 A g^{-1} (Fig. 8b) reveal excellent linearity and symmetry for all composites except pure MnO_2, indicating highly reversible charge storage kinetics. Critically, the 25 wt% MnO_2 electrode displays the smallest IR drop, highlighting the synergistic reduction of internal resistance at this optimal composition. This positive synergistic effect is further reflected in the specific capacitance trends. Analysis of gravimetric capacitance (Fig. 8c) confirms that pristine ACS-2.5 outperforms pure MnO_2 in both capacitance magnitude and rate capability. Remarkably, incorporating even a minor carbon fraction (25 wt% ACS-2.5 in the 75 wt% MnO_2 composite) elevates capacitance to levels approaching pristine ACS-2.5. Capacitance increases progressively with higher ACS-2.5 content, culminating in the 25 wt% MnO_2 composite achieving exceptional capacitance far exceeding all other electrodes—a clear manifestation of maximized synergistic enhancement. While composites with higher MnO_2 loading benefit from its superior compaction density, yielding improved initial volumetric capacitance, the 25 wt% MnO_2 electrode ultimately delivers the highest volumetric performance across tested conditions due to its outstanding gravimetric metrics as shown in Fig. 8d.

Electrochemical data for composites based on ACS-20 and ACS-10 are provided in Fig. S7 and S8 in SI. Table 3 summarizes the specific capacitance and rate capability metrics for all three ACS composites. A key distinction from lamellar ACs emerges: the optimal MnO_2 mass fraction for peak performance varies systematically with ACS sphere diameter. Specifically, larger sphere diameters necessitate higher MnO_2 loadings to achieve optimal electrochemical characteristics, demonstrating a direct correlation between carbon morphology and the composition-dependent synergy.

Fig. 9 comparatively assesses the electrochemical performance of hybrid electrodes based on three distinct carbon spheres (ACSs) at their respective optimal MnO_2 mass fractions. CV profiles recorded at 100 mV s^{-1} (Fig. 9a) demonstrate that all three composites retain well-defined quasi-rectangular shapes, characteristic of efficient capacitive behavior. Crucially, the enclosed CV area—a direct indicator of charge-storage capacity—increases progressively with decreasing carbon

Table 3 Specific capacitance and rate capability of ACS-*x* based composite electrode[a]

Sample	ACS-20			ACS-10			ACS-2.5		
	$C_{0.2}$			$C_{0.2}$			$C_{0.2}$		
MnO_2 wt%	C_g (F g^{-1})	C_v (F cm^{-3})	$C_{40}/C_{0.2}$	C_g (F g^{-1})	C_v (F cm^{-3})	$C_{40}/C_{0.2}$	C_g (F g^{-1})	C_v (F cm^{-3})	$C_{40}/C_{0.2}$
0	181.82 ± 5.45	96.36 ± 3.38	0.22 ± 0.01	266.66 ± 8.28	160.00 ± 4.31	0.22 ± 0.01	307.70 ± 9.23	212.31 ± 3.69	0.30 ± 0.01
25	235.30 ± 7.82	157.65 ± 6.10	0.36 ± 0.01	333.34 ± 10.25	246.67 ± 7.25	0.25 ± 0.01	430.44 ± 12.91	357.27 ± 7.87	0.61 ± 0.03
50	226.48 ± 6.79	178.92 ± 6.28	0.33 ± 0.02	356.00 ± 10.68	309.72 ± 9.18	0.44 ± 0.02	305.72 ± 9.17	293.49 ± 7.24	0.46 ± 0.02
75	240.00 ± 7.20	220.80 ± 7.76	0.45 ± 0.02	250.00 ± 7.62	247.50 ± 7.92	0.38 ± 0.03	250.00 ± 7.56	280.00 ± 7.71	0.39 ± 0.03
100	235.30 ± 8.12	296.48 ± 10.23	0.23 ± 0.01	235.30 ± 8.12	296.48 ± 10.23	0.23 ± 0.01	235.30 ± 8.12	296.48 ± 10.23	0.23 ± 0.01

[a] The "100 wt% MnO_2" refers to a pure MnO_2 electrode (*i.e.*, the "main electrode material" is 100% MnO_2, mixed with PTFE and carbon black in the fixed 80 : 15 : 5 ratio) and is the same across all AC samples, representing the average performance of this specific electrode.

sphere diameter, signifying enhanced specific capacitance in smaller particle systems. GCD curves at 4 A g^{-1} (Fig. 9b) reveal excellent symmetry and linearity across all composites, confirming reversible electrochemical processes. However, a systematic reduction in IR drop is observed with diminishing sphere size, most notably in the ACS-2.5 composite. This trend signifies lower internal resistance and improved charge-transfer kinetics in electrodes incorporating smaller carbon substrates. Gravimetric capacitance metrics as shown in Fig. 9c confirms the superior performance of the ACS-2.5 composite. While higher MnO_2 loadings in ACS-10 and ACS-20 electrodes enhance compaction density, the ACS-2.5 hybrid achieves exceptional volumetric capacitance, surpassing its counterparts through optimal synergy between high specific capacitance and moderate electrode density (Fig. 9d). Quantitative performance data in Table 3 highlight the exceptional metrics of the ACS-2.5/25 wt% MnO_2 composite with 430.44 F g^{-1} in gravimetric capacitance, 357.27 F cm^{-3} in volumetric capacitance, as well as 0.61 capacitance retention at 40 A g^{-1}, representing a competitively balanced electrochemical profile for practical supercapacitor applications.

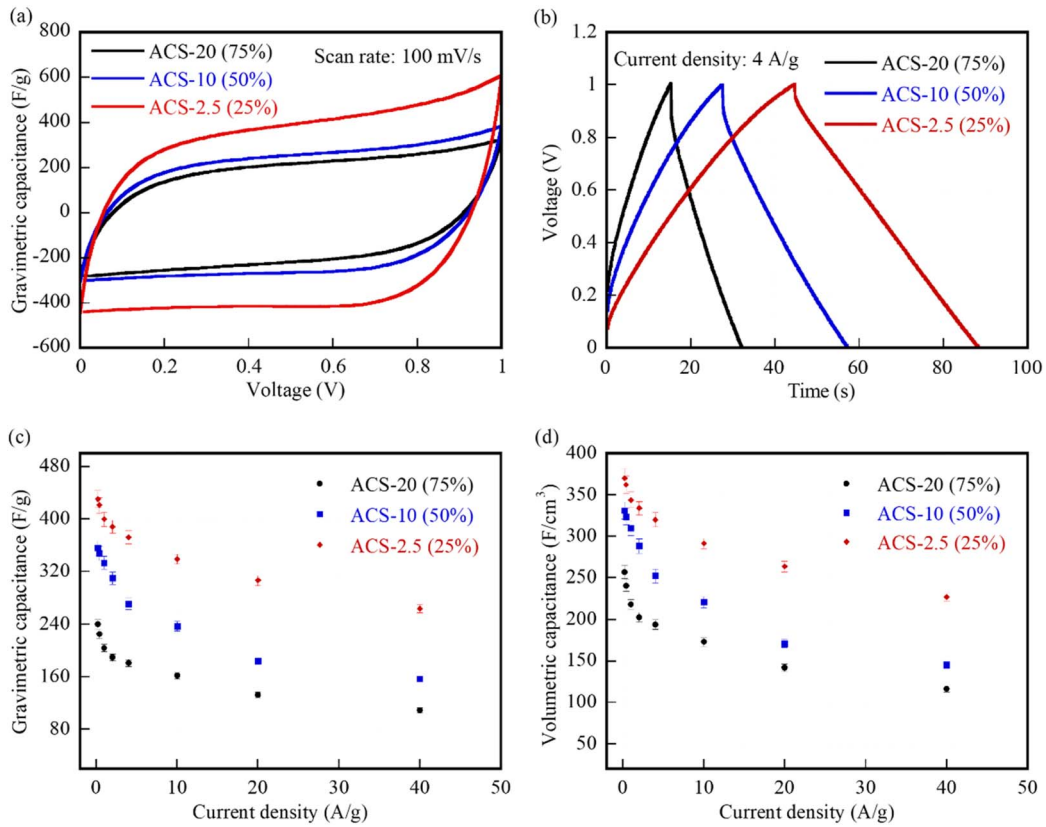

Fig. 9 Comparison of the electrochemical performances of ACS-*x*s-based composite electrode at optimum MnO_2 mass ratio: (a) CV curves at 100 mV s^{-1}, (b) GCD curves at 4 A g^{-1}, (c) variation of gravimetric capacitance with current density, and (d) variation of volumetric capacitance with current density.

Synergistic mechanism in AC/MnO_2 hybrid electrodes

The electrochemical characterization consistently demonstrates that the hybrid electrodes exhibit superior comprehensive performance at specific MnO_2 mass ratios—surpassing both pure activated carbon and pure MnO_2—indicating a distinct positive synergistic effect between the two components. A detailed investigation of the charge storage mechanism, including CV analysis at low (1–5 mV s^{-1}) and high (50–200 mV s^{-1}) scan rates (Fig. S9 in SI), revealed that while minor pseudocapacitive features can be detected at very low scan rates (1–5 mV s^{-1}), while the CV profiles at higher scan rates (50–200 mV s^{-1}) exhibit slender shapes, completely devoid of faradaic peaks, which is strikingly similar to that of microporous ACs at high scan rates, dictated by ion transport limitations rather than redox reactions.

Quantitative Dunn's analysis (Fig. S10 and Table S1) reveal that the kinetics are overwhelmingly dominated by diffusion-controlled processes, with *b*-values consistently near 0.525 and a negligible average capacitive contribution of only 2.4%. This presents a clear mechanistic dichotomy: the electrochemical signature suggests a double-layer-like behavior, yet the kinetics are diffusion-limited.

This apparent paradox may be resolved by considering the material's physicochemical properties. N_2 physisorption analysis (Fig. 3 and Table 1) shows that the MnO_2 possesses a significant specific surface area arising from a predominantly microporous structure (93.3% micropores). Concurrently, the EIS analysis (Table 4) provides direct kinetic evidence, showing a substantially larger Warburg time constant (W-T = 1.19 s) for the pure MnO_2 electrode compared to all composites. This combination of structural and electrochemical data leads to a definitive conclusion: the charge storage in pure MnO_2 is best described as a diffusion-limited electric double-layer formation, where ion transport within the constricted micropores becomes the rate-determining step. Hence, the primary function of MnO_2 in hybrid electrode is not to provide pseudocapacitance but to act as a multifunctional structural agent.

For lamellar ACs (*i.e.* AC-*xs*). The AC fragment contains intraparticle voids, while the irregular stacking of lamellae creates significant interparticle gaps, which impede efficient electron transport and ion diffusion. The MnO_2 fragments (as presented from Fig. 1h) mitigate these limitations through a dual mechanism, as directly visualized in the SEM-EDX maps of the AC-5/25% MnO_2 electrode (Fig. 1h): (1) as intraparticle bridges, the MnO_2 fragments infiltrate and fill the internal voids within carbon particles (highlighted by yellow circles), forming conductive pathways that enhance charge transfer. (2) As interlamellar spacers, they intercalate between AC sheets (highlighted by blue circles), which may reduce interparticle gaps and promote denser packing (Fig. 10a). The XRD patterns (Fig. 4c) confirm that this integration is a physical process, with no new phases formed, preserving the individual characteristics of both components. Furthermore, the hydrophilic surface of MnO_2 improves electrolyte wettability, while its nanostructured architecture facilitates ion transport. We propose that excessive MnO_2 may form thicker, more resistive interparticle layers, which could counteract the benefits of improved packing, as suggested by the increased charge transfer resistance (R_{ct}) observed in EIS analysis at higher MnO_2 loadings (Table 4).

For spherical ACSs. The regular morphology of carbon spheres inherently minimizes intraparticle porosity, restricting MnO_2 primarily to interparticle gaps. As shown in the SEM-EDX map for the ACS-2.5/25% MnO_2 composite (Fig. 1i), the MnO_2 fragments uniformly coat the spherical carbon surface and form interparticle bridges (blue circles). In small spheres (*e.g.*, ACS-2.5), tight packing is expected to minimize interparticle spaces, which could explain the requirement for a lower MnO_2 loading to achieve optimal performance. It is plausible that excessive MnO_2 in such systems not only introduces resistive pathways but might also disrupt the efficient packing of the carbon spheres. Conversely, larger spheres (*e.g.*, ACS-20) exhibit larger interparticle gaps, necessitating a higher MnO_2 content to achieve equivalent conductive bridging and densification effects. This size-dependent rationale aligns with the experimental trend of increasing optimal MnO_2 ratio with larger sphere diameter (Fig. 10b). The Raman spectra (Fig. 4f) further corroborate the successful physical combination of the two phases in the composites, showing the distinct signatures of

Table 4 Fitting parameters of Nyquist plots with equivalent circuit for AC-*xs*

	MnO_2 wt%	R_1 Ω	R_2 Ω	C_1 F	W_1-T s	W_1-P	CPE-T S s^P	CPE-P
AC-1	0	0.78	7.99	0.00021	0.86	0.45	0.22	0.92
	25	0.65	3.97	0.00025	0.52	0.45	0.23	0.93
	50	0.88	4.32	0.00018	0.74	0.43	0.18	0.92
	75	1.02	6.88	0.00011	1.08	0.41	0.14	0.91
AC-3	0	0.74	7.08	0.00024	0.58	0.46	0.26	0.93
	25	0.56	2.78	0.00026	0.32	0.46	0.27	0.93
	50	0.82	3.98	0.00022	0.36	0.47	0.22	0.92
	75	1.04	5.23	0.00017	0.88	0.43	0.18	0.9
AC-5	0	0.72	5.22	0.0003	0.18	0.48	0.28	0.95
	25	0.64	2.66	0.00033	0.12	0.49	0.33	0.96
	50	0.86	3.76	0.00025	0.22	0.45	0.25	0.93
	75	1.08	4.45	0.00018	0.56	0.44	0.19	0.91
MnO_2	100	1.26	11.64	0.0002	1.19	0.37	0.11	0.77

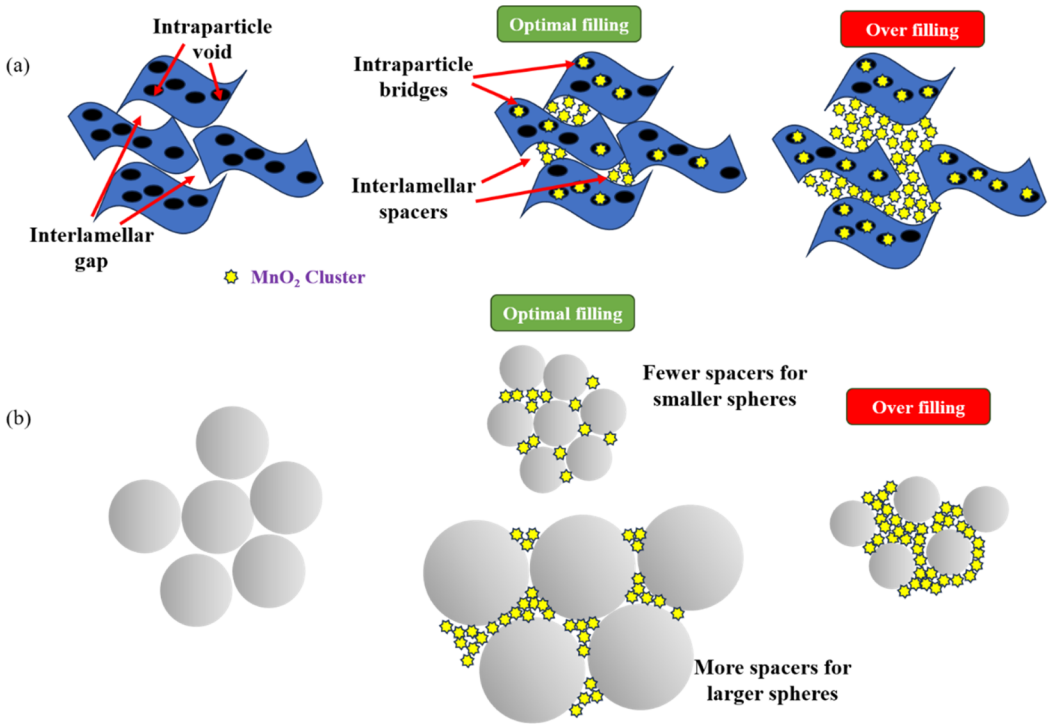

Fig. 10 Schematic illustration of synergetic effects t between MnO_2 and ACs for: (a) AC-*x*s and (b) ACS-*x*s.

both carbon and MnO_2 without evidence of chemical interaction.

In summary, the synergy may arise from multifunctional role of MnO_2 cluster in void-filling, conductive-bridge formation, and electrolyte modulation, with the optimal loading dictated by the host void architecture and stacking morphology of the ACs. This mechanistic understanding provides a universal framework for designing high-performance hybrid electrodes based on carbon–metal oxide composites.

To further elucidate the energy storage mechanism and synergistic effects within the composite electrodes, electrochemical impedance spectroscopy (EIS) was employed. The Nyquist plots of all composite electrodes, as depicted in Fig. 11, can be generally divided into three distinct regions. In the high-frequency region, a depressed semicircle is observed. The intercept of the semicircle with the real axis (Z') corresponds to the equivalent series resistance (ESR), which is primarily governed by the intrinsic resistance of the electrode materials, the electrolyte resistance, and the contact resistance at the electrode/electrolyte interface. The diameter of the semicircle represents the charge transfer resistance (R_{ct}), associated with charge transport within and between electrode particles, as well as the contact impedance between the active material and the current collector. The mid-frequency region is characterized by a linear segment with a slope of approximately 45°, indicative of ion diffusion and transport within the electrode (Warburg diffusion). In the low-frequency region, a more vertical "spike" suggests superior capacitive behavior and easier ion accessibility.

As shown in Fig. 11a, the pure MnO_2 electrode exhibits a significantly larger semicircle and a more inclined low-frequency line, indicating high overall impedance and poor capacitive performance. In contrast, the composite electrode incorporating AC-5 demonstrates a markedly reduced semicircle and a much more vertical spike, signifying decreased impedance and enhanced capacitance. The electrode with the optimal MnO_2 mass ratio (25 wt%) exhibits the most favorable Nyquist profile. A comparison of various AC-*x* samples at their optimal MnO_2 ratios (Fig. 11b) confirms that the AC-5-based composite achieves the best capacitive behavior, consistent with its highest specific capacitance and rate capability. Similarly, for the ACS-based composites (Fig. 11c and d), the EIS performance aligns with the electrochemical results, where the optimal MnO_2 mass fraction and ACS type (*i.e.* smaller spheres) correspond to the most ideal Nyquist plots, featuring lower impedance and more capacitive-like responses. Nyquist plots for other ACs with different MnO_2 ratios are provided in Fig. S11 (SI). Overall, the EIS results are in excellent agreement with the other electrochemical measurements, confirming the optimal MnO_2 content for each carbon type.

The experimental Nyquist plots were fitted using the equivalent circuit model shown in Fig. 11e, and the extracted parameters are summarized in Tables 4 and 5. The parameter R_1 (ESR) shows an increasing trend with higher MnO_2 loading, which is attributed to the relatively higher intrinsic resistance of MnO_2 compared to the ACs. Notably, the ESR values for different ACs (both lamellar ACs and ACSs) at the same MnO_2 ratio are quite similar, suggesting that the morphology and porous structure of the ACs have a negligible impact on the overall ESR of the composite electrodes. The resistance R_2 in the RC branch corresponds to the charge transfer resistance (R_{ct}). For the lamellar AC-*x* series, the minimum R_{ct} value is

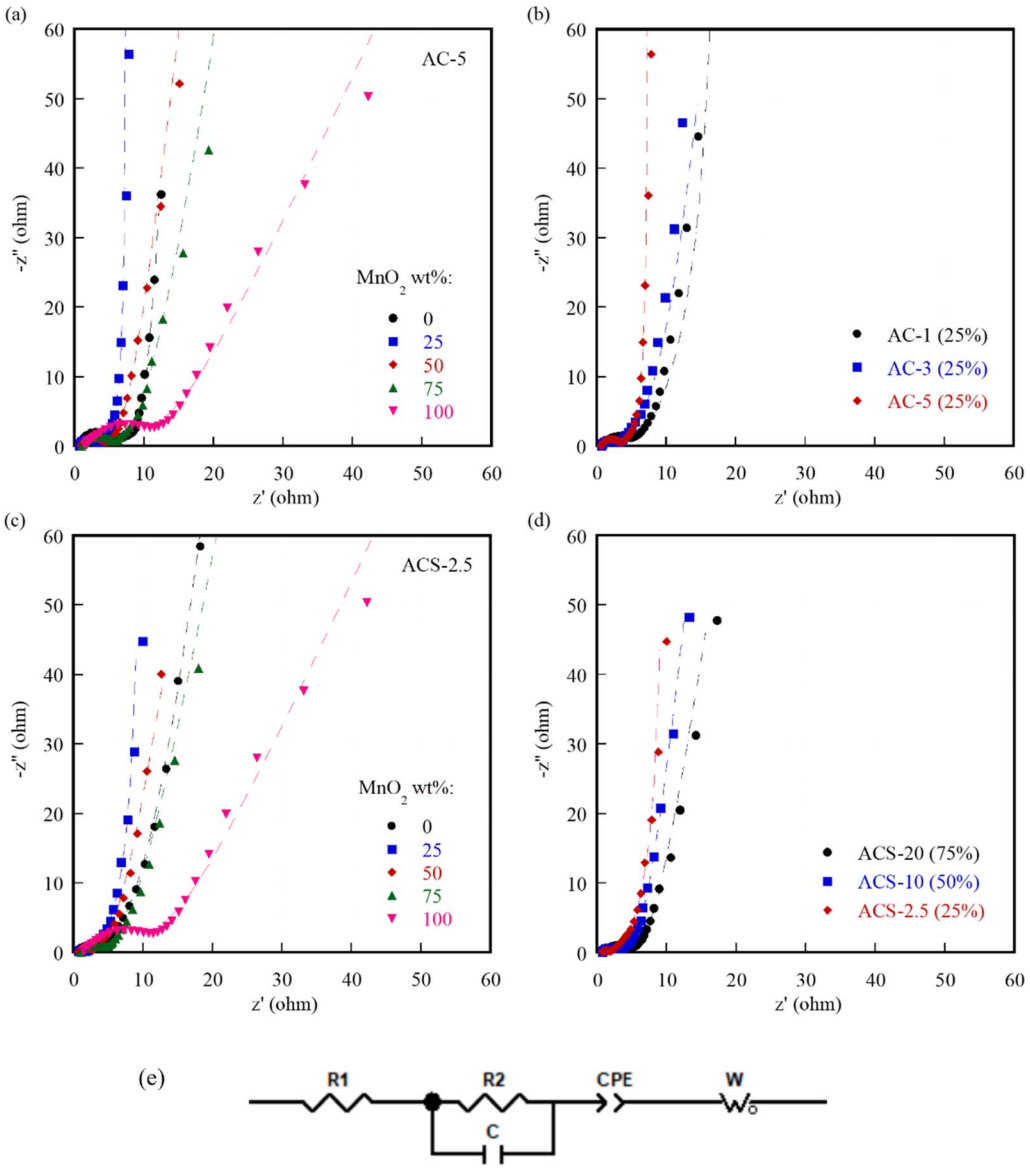

Fig. 11 Nyquist plots of: (a) AC-5/MnO_2 hybrid electrode in different MnO_2 mass ratios, (b) AC-*x*s/MnO_2 hybrid electrode with optimum MnO_2 mass ratios, (c) ACS-5/MnO_2 hybrid electrode in different MnO_2 mass ratios, (d) ACS-*x*s/MnO_2 hybrid electrode with optimum MnO_2 mass ratios; (e) equivalent circuit.

consistently observed at the optimal MnO_2 ratio (25 wt%), validating our hypothesis that a conformal MnO_2 "coating" on carbon particles facilitates charge transfer by improving inter-particle connectivity and providing efficient intraparticle pathways. Among the different AC-*x* types, the AC-5-based composite consistently exhibits the lowest R_{ct} at any given MnO_2 ratio, correlating with its superior capacitive performance. This is likely due to its favorable mesoporous structure (Table 1), which enhances ion transport. For the ACS series, ACS-10 and ACS-2.5 also show their minimum R_{ct} at their respective optimal MnO_2 ratios. However, ACS-20, likely due to disruption of tight sphere packing by an excessive MnO_2 coating, does not show a minimum R_{ct} at its optimal ratio, though the value remains relatively low compared to most other ratios. These findings underscore the positive role of a thin, conformal MnO_2 layer in enhancing charge transfer and the negative impact of an overly thick layer that impedes efficient carbon sphere packing.

The capacitance (C) in the RC branch represents the ideal electric double-layer capacitance (EDLC). The variation of the fitted C values follows a trend consistent with the experimental specific capacitances listed in Tables 2 and 3, reaching a maximum at the optimal MnO_2 ratio and for the best-performing carbon type.

For the intermediate-frequency range, a Warburg element (W) was incorporated into the circuit to describe ion diffusion. The Warburg exponent (W-P) is close to 0.5 for an ideal diffusion process. While the pure MnO_2 electrode shows a significant deviation from 0.5, all composite electrodes exhibit W-P

Table 5 Fitting parameters of Nyquist plots with equivalent circuit for ACSs

	MnO_2 wt%	R_1 Ω	R_2 Ω	C_1 F	W_1-T s	W_1-P	CPE-T S s^P	CPE-P
ACS-20	0	0.72	4.12	0.00016	0.51	0.45	0.091	0.88
	25	0.72	2.98	0.00019	0.29	0.44	0.12	0.91
	50	0.82	3.98	0.00017	0.32	0.45	0.14	0.9
	75	1.14	3.65	0.0002	0.25	0.46	0.18	0.91
ACS-10	0	0.69	2.84	0.00024	0.56	0.47	0.099	0.88
	25	0.78	2.61	0.00026	0.28	0.46	0.2	0.91
	50	0.84	2.56	0.00032	0.22	0.47	0.21	0.91
	75	1.04	4.43	0.00022	0.33	0.44	0.16	0.89
ACS-2.5	0	0.72	2.71	0.00032	0.24	0.48	0.16	0.93
	25	0.78	1.66	0.00039	0.092	0.5	0.27	0.95
	50	0.84	2.08	0.00031	0.12	0.46	0.24	0.95
	75	1.06	3.57	0.00022	0.22	0.45	0.2	0.93
MnO_2	100	1.26	11.64	0.0002	1.19	0.37	0.11	0.77

values near this ideal value, indicating efficient ion diffusion. The Warburg time constant (W-T) is smallest for electrodes at their optimal MnO_2 loading (Table 4), suggesting faster ion diffusion and transport. Comparing the AC-*x* samples, W-T decreases with increasing mesopore ratio (Table 1), confirming that a well-developed mesoporous network provides superior ion transport channels. Similarly, for the ACSs (Table 5), the optimal MnO_2 ratio and smaller sphere size (ACS-2.5) contribute to significantly improved ion transport kinetics.

The low-frequency capacitive behavior was modeled using a constant phase element (CPE). The CPE exponent (CPE-P) is influenced by electrode surface homogeneity, defects, and porosity, of which 1 represents an ideal capacitor. The pure MnO_2 electrode shows a low CPE-P value of 0.77, indicating its resistive nature. Composites with ACs show a dramatic increase in CPE-P, approaching ideal capacitive behavior. Among AC-*x* samples, the higher mesoporosity slightly enhances the CPE-P value. For the ACSs, the tighter packing of smaller spheres (ACS-2.5) results in a higher CPE-P. The optimal MnO_2 loading also contributes to a higher CPE-P value. The CPE modulus (CPE-T) generally follows the same trend as the specific capacitance.

In summary, the EIS analysis across high, medium, and low-frequency regions provides a comprehensive understanding of the synergistic effects between MnO_2 and ACs. The results consistently demonstrate that an appropriate MnO_2 addition significantly reduces charge transfer resistance, facilitates ion diffusion, and enhances capacitive behavior. These findings are in full agreement with the CV and GCD results, robustly confirming the above-proposed explanation for synergetic effects.

Long-term cycling life and energy density

The long-term cycling stability of the symmetric SCs assembled with the hybrid electrodes was evaluated by GCD testing at a current density of 10 A g^{-1} for 5000 cycles. The specific capacitance retention rates for the composites based on AC-*x* and ACSs, each at their optimal MnO_2 mass ratio, are presented in Fig. 12a and b, respectively. As shown, all composite electrodes demonstrated excellent cycling stability. Notably, the composite electrodes based on AC-5 and ACS-2.5 with the optimal 25 wt% MnO_2 loading achieved outstanding capacitance retention rates of 93.35 ± 0.46% and 93.41 ± 0.23%, respectively, after 5000 GCD cycles.

The coulombic efficiency remained consistently high, fluctuating between 99.5% and 99.9% throughout the entire testing period as shown in Fig. 12c and d. This near-unity coulombic efficiency indicates highly reversible charge–discharge processes with minimal side reactions, effectively ruling out significant Mn dissolution or other irreversible faradaic processes that would typically compromise coulombic efficiency.

To gain deeper insight into the structural stability of MnO_2, we conducted X-ray photoelectron spectroscopy (XPS) on a pure MnO_2 electrode before and after 5000 GCD cycles at 10 A g^{-1} (Fig. S12). The high-resolution Mn 2p spectra (Fig. S12a) exhibit the characteristic doublet of Mn $2p_{3/2}$ and Mn $2p_{1/2}$ at binding energies of 642.4 eV and 654.0 eV, respectively, along with a distinct satellite peak at 644.8 eV, which is a fingerprint of the Mn^{4+} state in birnessite-type MnO_2. Critically, the positions, shapes, and relative intensities of all these Mn 2p peaks remained virtually identical after 5000 cycles. Importantly, the composite electrode ACS-2.5/25% MnO_2 shows remarkably similar behavior (Fig. S11c). The Mn 2p spectra before and after cycling are nearly superimposable, demonstrating that the MnO_2 within the composite matrix maintains the same excellent chemical stability as the pure phase. This provides unequivocal evidence that the Mn oxidation state and the local chemical environment of MnO_2 were perfectly preserved in both configurations, ruling out significant phase transformation or reduction.

The O 1s spectra provide additional insights. The pure MnO_2 electrode (Fig. S12b) shows the lattice oxygen peak (Mn–O–Mn) at ~529.8 eV and a surface oxygen peak (–OH/H_2O) at ~532.0 eV that increases after cycling. In the composite electrode (Fig. S12d), we observe three distinct oxygen components: the MnO_2 lattice oxygen at ~529.8 eV, the MnO_2 surface oxygen at ~532.0 eV (which similarly increases after cycling), and an additional peak at ~533.5 eV characteristic of oxygen functional groups in the activated carbon matrix.[10] The stability of the MnO_2-related oxygen peaks in both electrodes, combined with

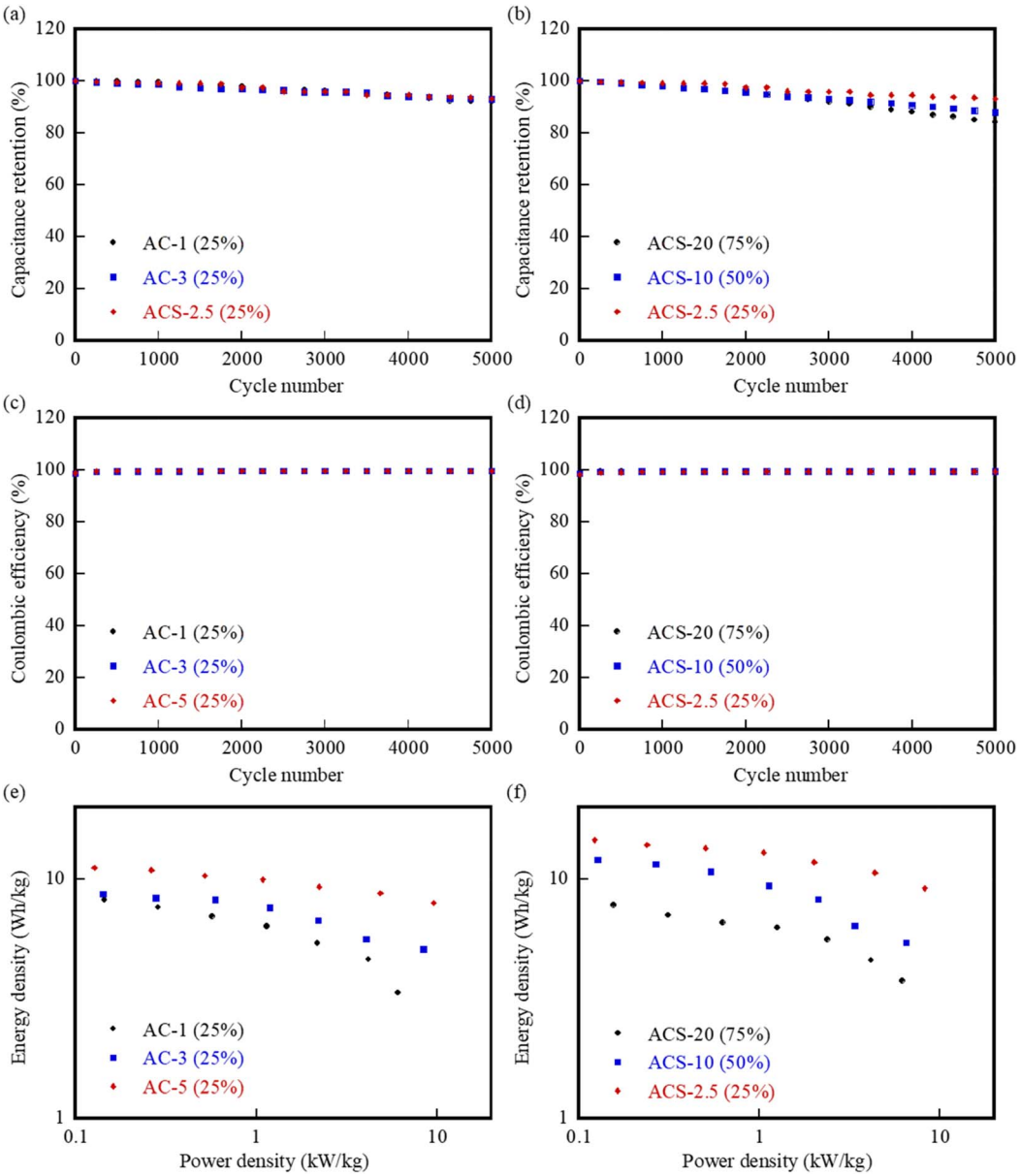

Fig. 12 Long-term cycling stability of: (a) AC-*x*s/MnO_2 hybrid electrode with optimum MnO_2 mass ratios, and (b) ACS-*x*s/MnO_2 hybrid electrode with optimum MnO_2 mass ratios; coulombic efficiency profiles of: (c) AC-*x*s/MnO_2 hybrid electrode with optimum MnO_2 mass ratios, and (d) ACS-*x*s/MnO_2 hybrid electrode with optimum MnO_2 mass ratios; Ragone plots of SCs for: (e) AC-*x*s/MnO_2 hybrid electrode with optimum MnO_2 mass ratios, and (f) ACS-*x*s/MnO_2 hybrid electrode with optimum MnO_2 mass ratios.

the unchanged carbon-related oxygen peak at ~533.5 eV in the composite, confirms that the bulk structures of both components remain intact during cycling.

This comprehensive XPS analysis demonstrates that the chemical environment and oxidation state of MnO_2 are identically preserved in both pure and composite configurations, validating the use of pure MnO_2 XPS as representative of its behavior within the composite. The consistent surface hydroxylation observed in both systems is a benign phenomenon that does not compromise the electrochemical performance.

The energy density (E) and power density (P) of the hybrid electrodes at their optimal MnO_2 ratios were calculated using eqn (3) and (4). The Ragone plots, depicted in Fig. 12c and 11d, reveal that the optimal AC-5-based composite electrode delivered a higher energy density than the other two lamellar AC-based composites. It achieved an energy density of 11.81 Wh kg^{-1} at a power density of 0.065 kW kg^{-1}, and maintained 7.95 Wh kg^{-1} at a high-power density of 9.54 kW kg^{-1}. The ACS-based composite electrodes exhibited even superior energy density performance. The ACS-2.5-based composite with the optimal 25 wt% MnO_2 loading achieved a high energy density of 14.96 Wh kg^{-1} at a power density of 0.061 kW kg^{-1} and retained 9.17 Wh kg^{-1} at 8.25 kW kg^{-1}. Given that aqueous supercapacitors typically operate within a narrow voltage window (0–

Table 6 Comparison of comprehensive electrochemical performances with the electrodes reported in literature

Electrode	Electrolyte	Current density	Specific capacitance (F g^{-1})	Rate capability	Cycling stability (cycles)	Energy density (Wh kg^{-1})	Power density (W kg^{-1})	Ref.
MnO_2/carbon nanotube	0.5 M Na_2SO_4	0.5 A g^{-1}	253.86	23.3% at 6 A g^{-1}	78.26% (6000)	32	413.7	31
MnO_2 composite WC electrode	0.02 M $KMnO_4$	1.0 mA cm^{-2}	87	—	75.2% (10 000)	12.2	22.3	45
MnO_2 with hierarchical nanostructures	1 M Na_2SO_4	3 mA cm^{-2}	304	52.7% at 30 mA cm^{-2}	108% (2000)	8.3 mWh cm^{-3}	0.28 W cm^{-3}	46
δ-MnO_2	0.5 M Na_2SO_4	0.25 A g^{-1}	190	—	~110% (500)	—	—	47
Low temperature synthesis of MnO_2	0.5 M Na_2SO_4	0.1 mA cm^{-2}	348.2	—	89% (2000)	43.3	2200	48
MnO_2/CNT	1 M KOH	0.5 A g^{-1}	405.5	22.2% at 5 A g^{-1}	108% (2000)	25	4800	49
MnO_2/carbon nanotubes	0.5 M Na_2SO_4	5 mV s^{-1}	348	65% at 20 A g^{-1}	91.3% (92.2)	19.2	6400	50
Carbon matrix decorated with MnO_2	1 M Na_2SO_4	1 A g^{-1}	197	77% at 10 A g^{-1}	95% (5000)	17.1	11 000	51
Carbon nanosheets/MnO_2/$NiCo_2O_4$	1 M KOH	0.5 A g^{-1}	161	93.1% at 5 A g^{-1}	81.9% (5000)	22.2	727.9	26
g-CN@MnO_2	2 M KOH	0.5 A g^{-1}	148.66	21.3% at 0.5 A g^{-1}	~50% (3000)	1.6	84	52
MnO_2/carbonaceous aerogel	6 M KOH	1 A g^{-1}	123.5	—	60% (1000)	—	—	53
MnO_2/CNTs	3 M KOH	2 A g^{-1}	199	50.8% at 77 A g^{-1}	97% (20 000)	—	—	54
V_2CT_x//MnO_2	PAM hydrogel	0.5 mA cm^{-2}	306 mF cm^{-2}	—	74.29% (15 000)	150 μWh cm^{-2}	470 μW cm^{-2}	55
MnOOH/MnO_2/CC	1 M Na_2SO_4	1 mA cm^{-2}	~248.2	20.8%	88.5 (10 000)	—	—	56
ACS-2.5/MnO_2	1 M KOH	0.2 A g^{-1}	430.44	61% at 40 A g^{-1}	93.41% (5000)	14.96	61	This work

1 V), resulting in energy densities generally between 5–10 Wh kg^{-1}, the composite electrodes developed in this work demonstrate excellent performance.

A comparison of the electrochemical performance between the composite electrodes developed in this study and those from recent reports on similar material systems is summarized in Table 6. The performance of our optimal dry-mixed ACS-2.5/MnO_2 (25%) electrode is highly competitive with, and in several aspects surpasses, that of composites fabricated by more intricate and less scalable methods. For instance, the dry-mixed electrode achieves a specific capacitance (430.44 F g^{-1}) higher than that of MnO_2/carbon composites prepared *via* electrodeposition,[31,46,54] grafting oxidation[50] and salt-template method.[53] More critically, our optimized dry-mixed electrode demonstrates superior performance to many other studies that also employed simple mixing techniques.[49,56] This decisive enhancement clearly indicates that the superiority of our work lies not merely in the use of dry-mixing, but in the strategic and morphology-guided optimization of the process. The common limitation of simple physical mixing—presumed poor and random interfacial contact—is effectively overcome in our design by tailoring the MnO_2 mass ratio to the specific void architecture (intraparticle *vs.* interparticle) of the carbon host. This work successfully shifts the performance driver from synthetic complexity to intelligent material selection and morphological design, establishing a practical and scalable paradigm for high-performance SC electrodes.

Conclusion

In summary, this work successfully demonstrates that a straightforward and scalable dry-mixing approach can fabricate high-performance MnO_2/AC composite electrodes, challenging the paradigm that complex chemical synthesis is necessary for achieving strong synergistic effects. Through meticulous design of ACs supports with well-defined lamellar and spherical morphologies, we have unraveled the profound influence of AC microstructure on the electrochemical behavior of the hybrids.

The central finding of this study is the establishment of a morphology–property relationship that governs the synergy. For lamellar ACs, a consistent optimal MnO_2 loading of 25 wt% was identified, where MnO_2 nanoparticles optimally fill intraparticle pores and form thin conductive layers between carbon sheets, significantly reducing charge-transfer resistance and enhancing ion diffusion. In contrast, for spherical ACSs, the optimal MnO_2 content is directly governed by the interparticle void volume, increasing with the sphere diameter. This distinction provides a framework for selecting carbon substrates based on their morphology to maximize synergy with metal oxides *via* simple mixing processes. The composite electrode based on mesoporous lamellar carbon (AC-5) with 25 wt% MnO_2 delivered excellent integrated performance, including a high gravimetric capacitance (340 F g^{-1} at 0.2 A g^{-1}) and superb rate capability (67% retention at 40 A g^{-1}). The ACS-2.5/25wt% MnO_2 composite achieved an even higher gravimetric capacitance of 430.44 F g^{-1}, outstanding cycling stability (93.41

± 0.23% retention after 5000 cycles) and an impressive energy density of 14.96 Wh kg^{-1}.

The EIS analysis provided quantitative evidence for the proposed mechanism, showing minimized R_{ct} and Warburg impedance at the optimal compositions. This study shifts the focus from novel material synthesis to the intelligent combination and mechanistic understanding of conventional materials. This work not only offers a cost-effective and scalable pathway for high-performance SC electrodes but also provides profound insights into the material-agnostic principles governing hybrid electrochemical systems.

We therefore envision that the composite material developed in this study demonstrates broad application potential in advanced portable systems, particularly for extended outdoor law enforcement operations. It is especially suited for powering devices such as police drones, body-worn cameras, specialized tactical equipment, and mobile training systems—applications where high energy and power delivery within a compact form factor is critically important. This positions our composite as a highly promising candidate for meeting the stringent energy demands of next-generation, field-deployable electronic devices.

Author contributions

Xuefei Cao: experimental design, writing – original draft. Xinran Liu: experiment. Qinglong Zou: data curation. Wei Sun: writing – review & editing, supervision.

Conflicts of interest

The authors declare that they have no known competing financial interests or personal relationships that could have appeared to influence the work reported in this paper.

Data availability

The data supporting the findings of this study are available upon request.

Supplementary information: XRD, Raman and N_2 adsorption–desorption data. See DOI: **https://doi.org/10.1039/d5ra06606a**.

Acknowledgements

This work is supported by the National Natural Science Foundation of China (No. 21805123), the Liaoning Revitalization Talents Program (XLYC1907067), the Fushun Revitalization Talents Program (FSYC202306002), National Key R&D Program of China Project (2020XXXX27102), and China Criminal Police University Research Project (Y2024078).

References

1 E. Frackowiak, Q. Abbas and F. Béguin, *J. Energy Chem.*, 2013, **22**, 226–240.
2 G. Wang, L. Zhang and J. Zhang, *Chem. Soc. Rev.*, 2012, **41**, 797–828.
3 K. Sun, X. Shi, X. Xie, W. Hou, X. Wang, H. Peng and G. Ma, *Int. J. Biol. Macromol.*, 2025, **286**, 138376.
4 H. Ji, X. Zhao, Z. Qiao, J. Jung, Y. Zhu, Y. Lu, L. L. Zhang, A. H. MacDonald and R. S. Ruoff, *Nat. Commun.*, 2014, **5**, 3317.
5 W. Sun, Y. Zhang, Z. Yang and F. Yang, *Int. J. Energy Res.*, 2020, **44**, 1930–1950.
6 K. Mazloomian, T. R. Dore, M. Buckwell, L. Bird, P. R. Shearing and T. S. Miller, *Energy Storage Mater.*, 2025, **76**, 104115.
7 S. Cui, W. Miao, X. Wang, K. Sun, H. Peng and G. Ma, *ACS Nano*, 2024, **18**, 12355–12366.
8 Y. Zhao, C. Qi, Q. Zou and W. Sun, *J. Energy Storage*, 2023, **73**, 109252.
9 C. J. Raj, R. Manikandan, M. Rajesh, P. Sivakumar, H. Jung, S. J. Das and B. C. Kim, *J. Power Sources*, 2021, **490**, 229518.
10 S. W. Wang, Z. X. Geng and W. Sun, *New J. Chem.*, 2023, **47**, 21411–21425.
11 B. Cheng, L. Wan, C. Du, H. Ye, Z. Tian and M. Xie, *J. Energy Storage*, 2024, **99**, 113259.
12 Y. Xiao, X. Y. Cai, W. Sun and F. Q. Yang, *J. Energy Storage*, 2022, **56**, 106040.
13 M. Xie, H. Meng, J. Chen, Y. Zhang, C. Du, L. Wan and Y. Chen, *ACS Appl. Energy Mater.*, 2021, **4**, 1840–1850.
14 C. An, Y. Zhang, H. Guo and Y. Wang, *Nanoscale Adv.*, 2019, **1**, 4644–4658.
15 Y. Liu, X. Xu, Z. Shao and S. P. Jiang, *Energy Storage Mater.*, 2020, **26**, 1–22.
16 M. Mastragostino, C. Arbizzani and F. Soavi, *J. Power Sources*, 2001, **97–98**, 812–815.
17 E. Vargun, H. Fei, U. Anik, Q. Cheng and P. Saha, *Mater. Chem. Phys.*, 2025, **344**, 131120.
18 M. Boota and Y. Gogotsi, *Adv. Energy Mater.*, 2019, **9**, 1802917.
19 M. A. A. Mohd Abdah, N. H. N. Azman, S. Kulandaivalu and Y. Sulaiman, *Mater. Des.*, 2020, **186**, 108199.
20 Y. Qiao, Y. Yu, Y. Jin, Y.-B. Guan and C.-H. Chen, *Electrochim. Acta*, 2014, **132**, 323–331.
21 A. G. Mahdy, A. A. Emam, E. A. Mussa, A. Y. Abdel-All, M. M. Rashad, A. M. Abuelftooh and S. G. Mohamed, *New J. Chem.*, 2023, **47**, 4418–4429.
22 W. H. Low, P. S. Khiew, S. S. Lim, C. W. Siong and E. R. Ezeigwe, *J. Alloys Compd.*, 2019, **775**, 1324–1356.
23 M. Huang, F. Li, F. Dong, Y. X. Zhang and L. L. Zhang, *J. Mater. Chem. A*, 2015, **3**, 21380–21423.
24 A. Saeed, H. Hassan, A. Hakami, H. Saad, K. Masood, M. W. Iqbal and S. Mumtaz, *New J. Chem.*, 2025, **49**, 3078–3088.
25 R. Yuksel and H. E. Unalan, *Int. J. Energy Res.*, 2015, **39**, 2042–2052.
26 X. D. Hong, C. Y. Deng, X. Wang, W. Dong and B. Liang, *J. Energy Storage*, 2022, **53**, 8.
27 P. Tagsin, P. Suksangrat, P. Klangtakai, P. Srepusharawoot, C. Ruttanapun, P. Kumnorkaew, S. Pimanpang and V. Amornkitbamrung, *Appl. Surf. Sci.*, 2021, **570**, 151056.

28 W. H. Tian, P. G. Ren, X. Hou, R. Z. Xue, Z. Y. Chen, Z. Z. Guo, Y. L. Jin and F. Ren, *Int. J. Biol. Macromol.*, 2024, **261**(Part 2), 129977.
29 M. J. Raei, M. Trifkovic, E. P. L. Roberts and G. Natale, *ACS Appl. Energy Mater.*, 2025, **8**(15), 10822–10832.
30 T. Yue, B. Shen and P. Gao, *Renewable Sustainable Energy Rev.*, 2022, **158**, 112131.
31 Z. Li, D. Xiao, C. Xu, Z. Li, S. Bi, H. Xu, H. Dou and X. Zhang, *J. Mater. Sci.*, 2022, **57**, 8818–8827.
32 T. Feng, Y. F. Mo, B. W. Zou, C. H. Zhang, H. Chen and G. Liu, *Carbon Lett.*, 2025, **35**, 1139–1151.
33 T. Le, Y. Yang, L. Yu, Z.-h. Huang and F. Kang, *Sci. Rep.*, 2016, **6**, 37368.
34 S. Dong, Z. Y. Wang, J. L. Wang, Y. Yao and H. F. Liu, *Mater. Express*, 2020, **10**, 1308–1316.
35 H. H. Zhang, J. N. Gu, Y. Y. Jiang, J. Zhao, X. X. Zhang and C. Y. Wang, *J. Solid State Electrochem.*, 2014, **18**, 235–247.
36 X. Fan, X. Wang, G. Li, A. Yu and Z. Chen, *J. Power Sources*, 2016, **326**, 357–364.
37 P. R. Jadhav, M. P. Suryawanshi, D. S. Dalavi, D. S. Patil, E. A. Jo, S. S. Kolekar, A. A. Wali, M. M. Karanjkar, J. H. Kim and P. S. Patil, *Electrochim. Acta*, 2015, **176**, 523–532.
38 Y. Li, X. Yan, Z. Cui, J. Yuan, B. Xu and G. Yang, *Adv. Mater. Interfaces*, 2025, **12**, 2400450.
39 H.-R. Shin, S.-J. Yeo, J.-H. Kim, D. Lee, B. Park, D.-J. Kwon and M. Kim, *Fibers Polym.*, 2025, **26**, 4737–4751.
40 W. Sun, Y. Zhang and F. Yang, *Electrochim. Acta*, 2020, **357**, 136874.
41 W. Sun, Y. L. Zhang, Z. X. Yang and F. Q. Yang, *Int. J. Energy Res.*, 2020, **44**, 1930–1950.
42 J. Wang, D. Zhang, F. Nie, R. Zhang, X. Fang and Y. Wang, *Environ. Sci. Pollut. Res.*, 2023, **30**, 15377–15391.
43 N. Bonini, M. Lazzeri, N. Marzari and F. Mauri, *Phys. Rev. Lett.*, 2007, **99**, 176802.
44 V. Thapliyal, M. E. Alabdulkarim, D. R. Whelan, B. Mainali and J. L. Maxwell, *Diamond Relat. Mater.*, 2022, **127**, 109180.
45 L. Chen, F. Wang, Z. Tian, H. Guo, C. Cai, Q. Wu, H. Du, K. Liu, Z. Hao, S. He, G. Duan and S. Jiang, *Small*, 2022, **18**, 2201307.
46 Z.-H. Huang, Y. Song, D.-Y. Feng, Z. Sun, X. Sun and X.-X. Liu, *ACS Nano*, 2018, **12**, 3557–3567.
47 J. M. d. O. Cremonezzi, D. Y. Tiba and S. H. Domingues, *SN Appl. Sci.*, 2020, **2**, 1689.
48 Y. Kumar, S. Chopra, A. Gupta, Y. Kumar, S. J. Uke and S. P. Mardikar, *Mater. Sci. Energy Technol.*, 2020, **3**, 566–574.
49 G. Srivastava, Ravina, S. Dalela, N. K. Gautam, S. Kumar, S. Z. Hashmi, M. A. Ahmad, A. M. Quraishi, V. Khanna and P. A. Alvi, *Nano Trends*, 2025, **9**, 100067.
50 J.-W. Wang, Y. Chen and B.-Z. Chen, *J. Alloys Compd.*, 2016, **688**, 184–197.
51 X. Y. Du, C. X. Hou, H. Kimura, X. B. Xie, H. Y. Jiang, X. Q. Sun, X. Y. Yang, Y. P. Zhang and W. Du, *J. Energy Storage*, 2023, **72**, 11.
52 M. Shin, K. P. Sharma, K. Kim, G. P. Awasthi and C. Yu, *J. Phys. Chem. Solids*, 2023, **177**, 10.
53 P. Su, W. Pei, X. Wang, Y. Ma, Q. Jiang, J. Liang, S. Zhou, J. Zhao, J. Liu and G. Q. M. Lu, *Angew. Chem.*, 2021, **60**, 16044–16050.
54 H. Zhang, G. Cao, Z. Wang, Y. Yang, Z. Shi and Z. Gu, *Nano Lett.*, 2008, **8**, 2664–2668.
55 S. Xiong, X. Li, G. Li, Z. Wang, Z. Wang, M. Guo, C. Zhang, Y. Ma and T. Zeng, *Adv. Funct. Mater.*, 2025, e13738.
56 Y. Liu, Z. Tian, P. Zuo, Z. Wan, Z. Chen, J. Yang, M. Ren, X. Qi, P. Hu, F. Teng and H. Fan, *J. Energy Storage*, 2025, **134**, 118121.